Materials Today Bio 16 (2022) 100334

Contents lists available at ScienceDirect

Materials Today Bio

journal homepage: www.journals.elsevier.com/materials-today-bio

Functionalizing multi-component bioink with platelet-rich plasma for customized *in-situ* bilayer bioprinting for wound healing

Ming Zhao [a,1], Jing Wang [a,1], Jinxin Zhang [b], Jingman Huang [a,c], Liang Luo [a], Yunshu Yang [a], Kuo Shen [a], Tian Jiao [d], Yanhui Jia [a], Weilong Lian [d], Jin Li [a], Yunchuan Wang [a,**], Qin Lian [d], Dahai Hu [a,*]

[a] Department of Burns and Cutaneous Surgery, Xijing Hospital, Fourth Military Medical University, Xi'an, Shaanxi, 710032, China
[b] Department of Emergency, Xijing Hospital, Fourth Military Medical University, Xi'an, Shaanxi, 710032, China
[c] No. 6 Cadet Regiment of Basic Medical School, Fourth Military Medical University, Xi'an, Shaanxi, 710032, China
[d] State Key Laboratory for Manufacturing Systems Engineering, School of Mechanical Engineering, Xi'an Jiaotong University, Xi'an, Shaanxi, 710054, China

ARTICLE INFO

Keywords:
Platelet-rich plasma
In-situ bioprinting
Skin substitute
Wound healing
Cell-laden scaffold
Individualized protein therapy

ABSTRACT

In-situ three-dimensional (3D) bioprinting has been emerging as a promising technology designed to rapidly seal cutaneous defects according to their contour. Improvements in the formulations of multi-component bioink are needed to support cytocompatible encapsulation and biological functions. Platelet-rich plasma (PRP), as a source of patient-specific autologous growth factors, exhibits capabilities in tissue repair and rejuvenation. This study aimed to prepare PRP-integrated alginate-gelatin (AG) composite hydrogel bioinks and evaluate the biological effects *in vitro* and *in vivo*. 3D bioprinted constructs embedded with dermal fibroblasts and epidermal stem cells were fabricated using extrusion strategy. The integration of PRP not only improved the cellular behavior of seeded cells, but regulate the tube formation of vascular endothelial cells and macrophage polarization in a paracrine manner, which obtained an optimal effect at an incorporation concentration of 5%. For *in-situ* bioprinting, PRP integration accelerated the high-quality wound closure, modulated the inflammation and initiated the angiogenesis compared with the AG bioink. In conclusion, we revealed the regenerative potential of PRP, readily available at the bedside, as an initial signaling provider in multi-component bioink development. Combined with *in-situ* printing technology, it is expected to accelerate the clinical translation of rapid individualized wound repair.

1. Introduction

The skin is the largest organ of the human body, playing a role in maintaining the fluids and electrolytes homeostasis, resisting physical and chemical damage, as well as preventing microbial infections [1,2]. Regrettably, full-thickness skin defects are prone to occur under various injury factors, such as large-scale burns, traumatic injuries, diabetic ulcers, and vascular lesions, which seriously harmed not only the life quality of patients, but also the medical economy [3]. Current therapeutic interventions remain far from ideal repair. The urgent clinical needs lie in overcoming the inadequate supply of donor skin grafts and the poor quality of tissue repair, which prompts the development of novel skin substitutes.

3D bioprinting has emerged as a promising bio-manufacturing strategy that could accurately position components including living cells and ECM in a designated 3D tissue via a rapid prototyping and layered manufacturing along planned paths, thereby constructing multicellular tissues/organs [4,5]. It facilitates the realization of complex topological structures through computer-aided design, regulating cell distribution and growth in a spatially controlled manner; grids between printed

* Corresponding author.
** Corresponding author.
E-mail addresses: Zhaom1690495777@163.com (M. Zhao), Tattewj@sina.com (J. Wang), 772116539@qq.com (J. Zhang), 1178951890@qq.com (J. Huang), clayluo@outlook.com (L. Luo), yangys0815@qq.com (Y. Yang), 1255725433@qq.com (K. Shen), 459508520@qq.com (T. Jiao), yanhui1230@163.com (Y. Jia), 773274210@qq.com (W. Lian), 707298682@qq.com (J. Li), wangyunchuan@fmmu.edu.cn (Y. Wang), lqiamt@mail.xjtu.edu.cn (Q. Lian), hudahaidoc@163.com, hudhai@fmmu.edu.cn (D. Hu).
[1] Authors contribute equally.

https://doi.org/10.1016/j.mtbio.2022.100334
Received 16 March 2022; Received in revised form 1 June 2022; Accepted 16 June 2022
Available online 24 June 2022
2590-0064/© 2022 The Authors. Published by Elsevier Ltd. This is an open access article under the CC BY-NC-ND license (http://creativecommons.org/licenses/by-nc-nd/4.0/).

microfilaments could create more space for cell proliferation, migration, and nutrient penetration [6]. 3D bioprinted skin substitutes have a strictly layered structure and controlled positioning of cell type and density, enhancing the homology with human natural skin [7].

Traditional 3D printing is performed on flat substrates based on plane layering. However, in actual clinical practice, the base of the wound is usually uneven and irregular. *In-situ* bioprinting is an on-site printing strategy that directly deposits cells and biomaterials on the defect after scanning morphological features of the wound after debridement [8]. 3D scanning of defect geometry dimensions makes it possible for individualized treatment of wounds. It facilitates real-time printing directly on the patient in a surgical setting with high anatomical precision [9], guiding the spatial control of bioink deposition to enable the construction of customized scaffolds that conform to the unique topology of each wound [10]. The human body was served as an "*in vivo* bioreactor" in this strategy [11]. Eliminating costly and time-consuming *in vitro* differentiation and multiple surgical procedures, it is appropriate for automated and standardized clinical applications. However, the *in-situ* deposition and functionalization put forward higher criterions for bioinks.

The bioinks was usually defined as a formulation of cells suitable for processing by an automated biofabrication technology that may also contain biologically active components and biomaterials. With the definitions in mind, biomaterials that qualify as a bioink could serve as a cell-delivery medium during formulation and processing [12]. Cell-laden bioinks should be optimized to meet certain key characteristics including rheological properties, physico-mechanical properties, and biofunctionality, which are hard to achieve with a single-component bioink [13]. Andrew et al. proposed that seeded cells, biological materials, and other additives together constitute the bioink [14]. As such, recent researches have been centered on component additives within multi-component bioinks to balance the biocompatibility and rheological properties [15].

Among the plentiful biomaterials, gelatin (Gel) and sodium alginate (Alg) have drawn extensive attention in biofabrication. Previously, our group has been committed to optimize the extrusion direct-writing printing process for them as a composite bioink [16,17]. Gelatin could be quickly gelled with temperature changes or with the participation of transglutaminase (TG) enzymes and the internal spatial structure could maintain for a long time. The incorporation of sodium alginate could improve the overall printability of the composite hydrogel (AG) [18], but it exhibits relatively inert to cells, lacking attachment sites for cell adhesion and migration. There is much room for improvement in cell compatibility and biological activity.

Platelet-rich plasma (PRP) is the plasma containing high concentrations of platelets (PLTs) obtained after centrifugations of whole blood [19]. High concentrations of PLTs could accelerate the hemostatic process by promoting the thrombosis and coagulation in wounds. Besides, α-particles of PLTs could release multiple supraphysiological concentrations of growth factors and other bioactive molecules (such as miRNA, chemokines, and immunoglobulins) [20], exhibiting excellent synergistic effects and avoiding the disadvantages of applying a single type of growth factor. Therefore, it has been utilized in areas of cutaneous wound repair [21], skin appendages regeneration [22] and rejuvenation [23,24], etc. Recent studies have reported that treatment with PRP in regenerative plastic surgery is associated with increased survival of transplanted adipose tissue [25]. Furthermore, as the importance of personalized medicine becomes more explicit, there have risen emerging needs to develop bioinks containing autologous/patient-specific bioactive factors [26]. As a source of patient-specific autologous growth factors, PRP could be easily integrated into hydrogels and printed into 3D structures [27]. Due to slow-release effect, it's expected to act continuously on the wound and initiate regenerative signals [28].

On account of the unique characteristics of skin structure, the layered fabrication of dermis and epidermis is particularly important for 3D printed skin substitutes. During normal wound healing, dermal fibroblasts (DFs) and epidermal stem cells (ESCs) play a dominant role in the repair of the dermis and epidermis, respectively, in cooperation with signaling molecules such as growth factors [29]. DFs participate in the formulation of granulation tissue and synthesis of extracellular matrix (ECM) [30]. ESCs migrate and differentiate to complete re-epithelialization. Therefore, DFs and ESCs were selected as seeded cells to mimic the dermis and epidermis in layered skin substitutes.

In this study, we prepared PRP as an additive to compose PRP-integrated AG composite hydrogel bioinks (AG-PRPs). DFs and ESCs-laden 3D bioprinted constructs were fabricated according to a single-layer or double-layered structure to investigate the regulatory effect of PRP on seeded cells and other wound healing-related effector cells *in vitro*. Furthermore, the AG-PRPs was utilized for *in-situ* extrusion bioprinting on full-thickness rat cutaneous defects via the robotic arm-based additive manufacturing system previously established by our group, in order to explore its functional outcomes in inflammation regulation, collagen synthesis, vascularization, and other processes (Fig. 1).

2. Methods

2.1. Patients and animals

All experimental protocols were approved under the guidelines of the Medical and Ethics Committee of Xijing Hospital, the Fourth Military Medical University (FMMU, Xi'an, China) and all animal studies were approved by the Animal Care and Use Committee of the FMMU. All patients were informed of the purpose and procedures of this study and agreed to offer their excised tissues. Written consents were obtained before surgery. SPF Sprague-Dawley rats were obtained from the Experimental Animal Center of the FMMU and kept under standard conditions with access to food and water ad libitum.

2.2. Cell culture and PRP preparation

For human primary DFs (HDFs) and ESCs (HESCs) isolation, human foreskin tissue was obtained from 6 patients (age range 8–33 years) undergoing circumcision. The cells were separated as previously described [31] and used at passage 3 to 4 for HDFs and passage 1 to 2 for HESCs in the following experiments. The above cells from rats was isolated from the dorsal skin of newborn (0–3 days) SD rat with a similar process. The ESCs were cultured in keratinocyte serum-free medium (KSFM; Gibco, USA) and identified with CK49fbri (Biolegend, USA), and CD71dim (Biolegend, USA) by flow cytometry.

A two-step centrifugation protocol was applied for preparation of allogeneic PRP (Fig. 2A). Briefly, fresh venous blood was collected from the patients or SD rats anticoagulated with 3.2% sodium citrate. The centrifugations were started within 20 min to maintain high bioactivity of growth factors and cytokines. The top and middle layers were transferred into a new sterile centrifuge tube after the first centrifugation at 900 *g*, 4 °C for 5 min, followed by the second centrifugation at 1500 *g*, 4 °C for 15 min. The redundant superficial layer of platelet-poor plasma was discarded while the remained part was gently suspended as the PRP with a yield of 20%. The blood cell count of whole blood and PRP products was detected by a five-segment blood cell analyzer (Mindray, China).

2.3. Materials and bioink pre-hydrogel precursor preparation

The bioinks was configured as shown in Fig. 4A. Briefly, gelatin particles (Sigma-Aldrich, USA) were dissolved in PBS and filtered with 0.22 μm filters (Millipore, Germany). After adding autoclaved Alg (Sigma-Aldrich, USA) powders, it's magnetically stirred at 80 rpm under a 37 °C water bath overnight to dissolve the Alg completely. Different concentrations of PRP (0, 2, 5, and 10%) were then incorporated and designated as AG, AG-2P, AG-5P, and AG-10P, respectively. Subsequently, digested and resuspended cells were mixed in. Bioink A contained HDFs with a density of 1×10^6/ml and Bioink B contained HESCs

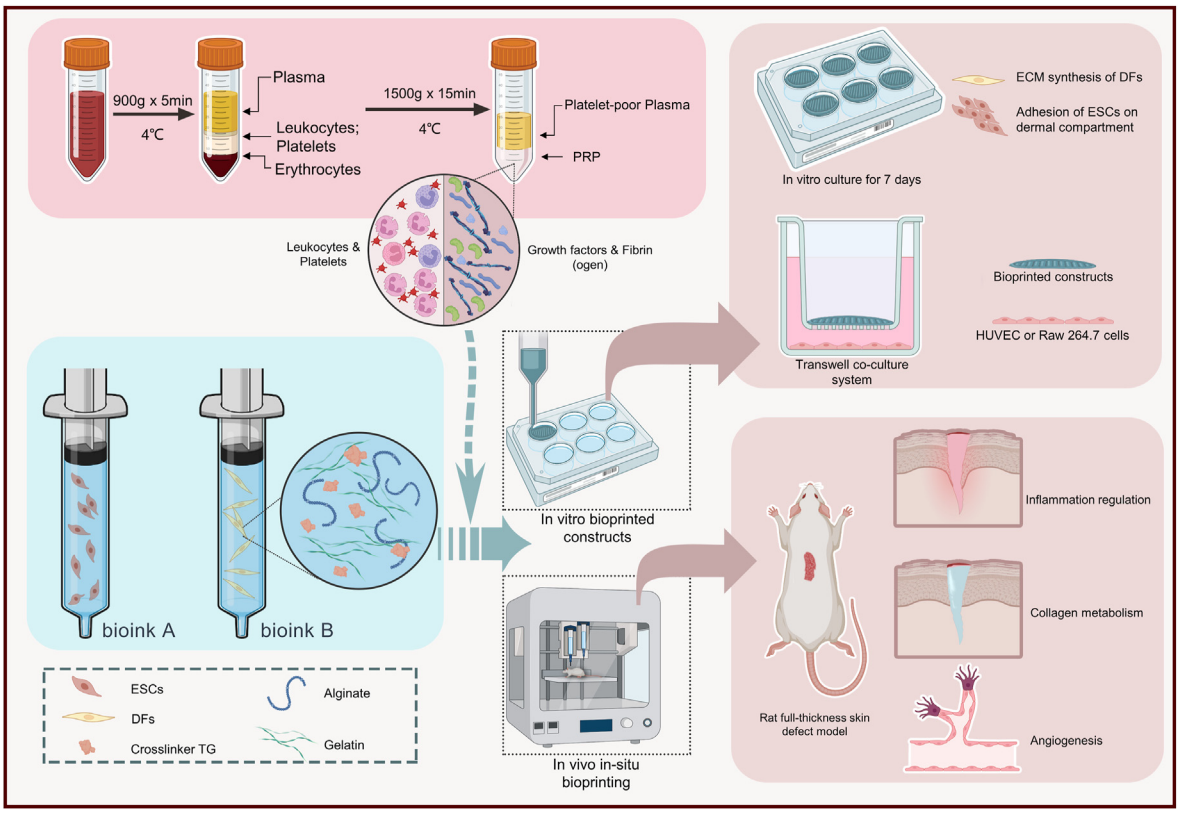

Fig. 1. Schematic illustration of bioprinting process using PRP containing multi-component bioink.

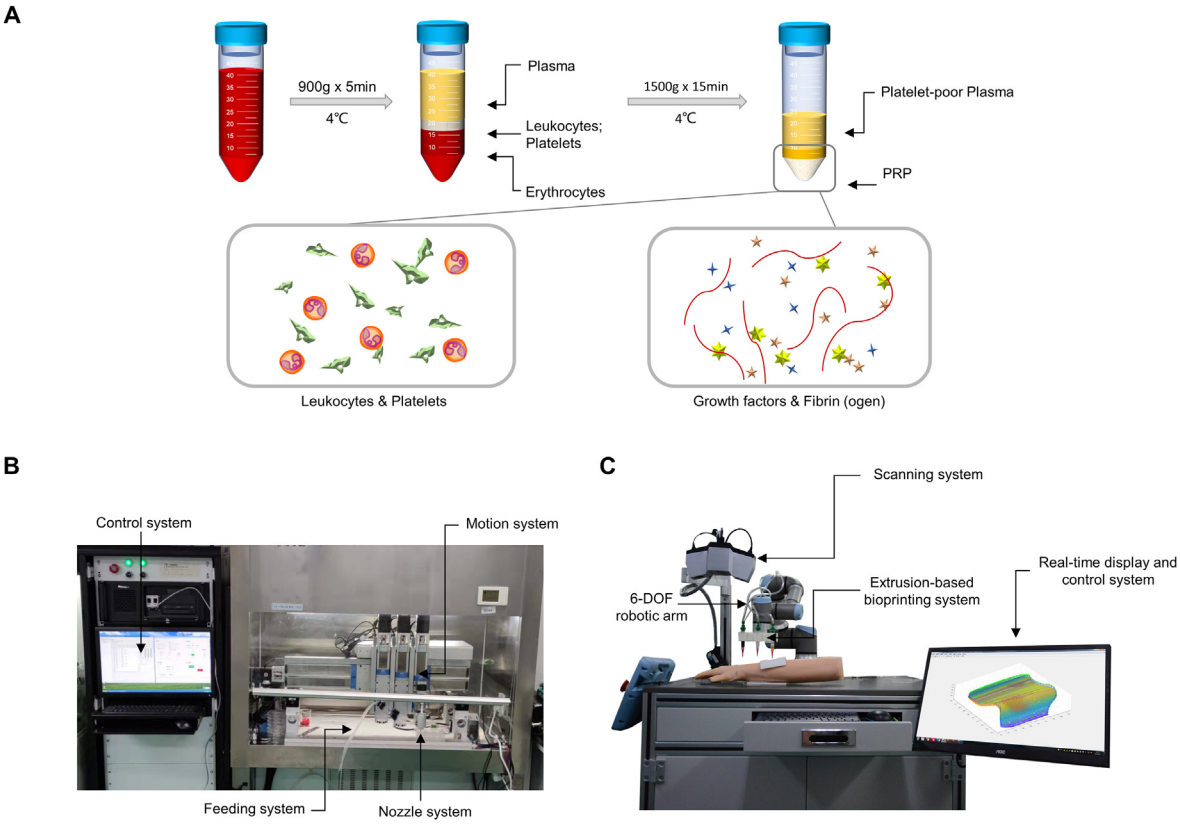

Fig. 2. The PRP preparation and 3D bioprinting devices. (A) Schematic diagram of PRP preparation; (B) The equipment for *in vitro* extrusion-based 3D bioprinting; (C) The robotic arm-based equipment for *in-situ in vivo* extrusion-based 3D bioprinting.

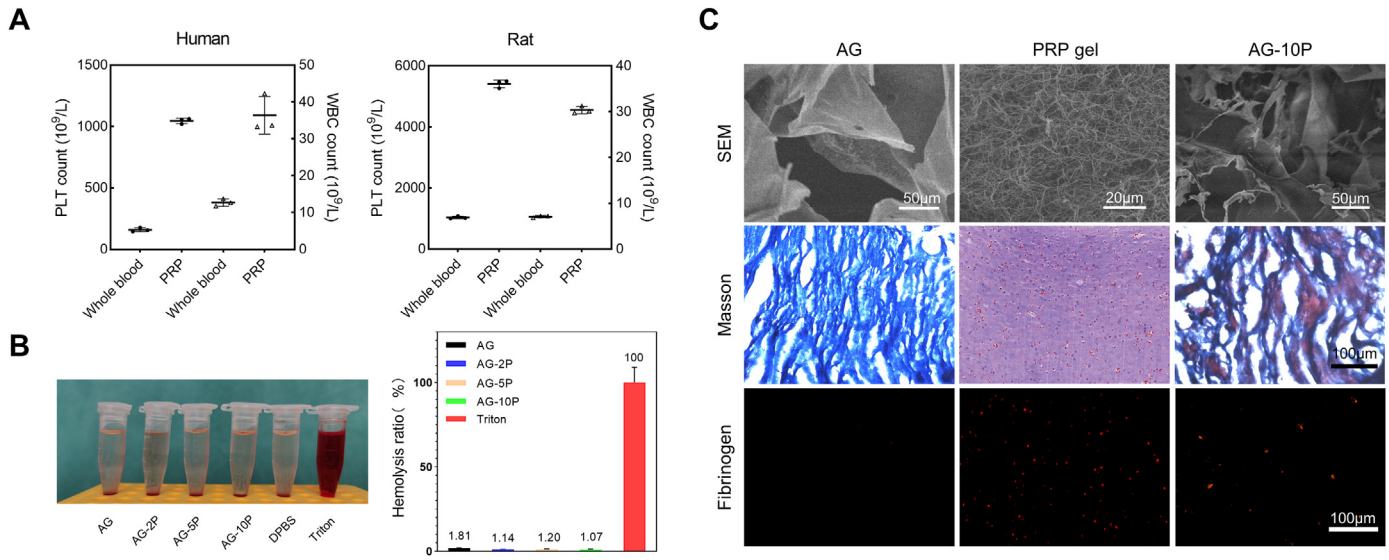

Fig. 3. Construction and characterization of PRP-incorporated composite hydrogels. (A) Identification of PRP by blood cell count. Data are expressed as the mean ± SEM; n = 6. (B) Direct contact hemolytic activity of composite bioink. Data are expressed as the mean ± SEM; n = 3. (C) The integration of PRP into AG hydrogel network characterized by SEM, Masson staining and immunofluorescent staining against fibrinogen.

with a density of 1×10^7/ml (or RDFs and RESCs for *in-situ in vivo* bioprinting experiments).

2.4. Assessment on rheology and hemocompatibility of bioinks

A DHR-2 rheometer (TA, USA) was used to analyze the rheological property of inks with different PRP concentrations following a reported method [32]. Temperature sweep test was implemented on hydrogel Sample AG-pre at 15–40 °C with a sweeping speed of 1 °C/min. After the mixture of TG, the stiffness of hydrogel Samples AG, AG-2P, AG-5P, and AG-10P were measured by time-sweep oscillatory tests. Viscosity was measured at shear rate from 1 to 100 s^{-1}. For peak hold tests, the shear rate was initially held at 0.75 s^{-1} for 60 s at 31 °C; then, the shear rate was increased to 300 s^{-1} for 5 s; then, the shear rate was dropped to 0.2 s^{-1} and temperature was dropped to 25 °C for 180 s.

The hemocompatibility of the AG-PRPs was assessed by direct contact with red blood cells as previously described [33]. Cell-free hydrogel precursors crosslinked by TG served as the experimental groups. The 0.1% Triton X-100 was used as the positive control and DPBS as a blank group.

2.5. Bioprinting fabrication process

2.5.1. Bioprinting for in vitro experiments

A custom-made extruded 3D printing equipment (Fig. 2B) was utilized to fabricate the single-layer membrane and double-layered skin substitutes *in vitro*. It was composed of a control system, a motion system, and a feed and temperature-controlled nozzle system. The main body of the equipment was in a sterile clean bench. The effective printing range was 100 × 100 × 100 mm, with a repeatable precision of 0.05 mm. A day before cell printing, the device, tabletop and the consumables were disinfected with 75% alcohol and irradiated with UV light for 12 h.

TG (BomeiBio, China), which applied as a crosslinking agent, was added to a final concentration of 1 wt% to the aseptically prepared Bioink A or Bioink B. A layer of HDFs or HESCs-embedded membrane measuring 15 × 15 × 0.3 mm was printed according to the parameters in Table 1 (Supplementary Video. 1). For double-layered skin substitutes printing, the HESCs and HDFs were labeled with PKH-67 and PKH 26 dyes (Sigma-Aldrich, USA) respectively in advance to observe the cell positioning. After the bioprinting is completed, the constructs were immersed with complete culture medium and let stand at room temperature for 15 min for the maintenance of printed form and the complete enzymatic cross-link. Then they were cultured *in vitro* at 37 °C in 5% CO2 for 7 days.

Supplementary video related to this article can be found at https://doi.org/10.1016/j.mtbio.2022.100334

2.5.2. In-situ bioprinting for in vivo experiments

A robotic arm-based hydrogel additive manufacturing system was applied for *in-situ* bioprinting (Fig. 2C). It's composed of the scanning system and the printing system. The former consists of a commercial binocular scanner (XTOM, China), while the latter consists of a 6-DOF robotic arm (Universal Robots), an extrusion-based bioprinting unit, and a real-time display and control system. The anesthesia of the rats and the preparation of cutaneous wound model were carried out as described in Part 2.10 below. The skin defects were then scanned by the scanning system. 3D point cloud data with depth of skin defect were obtained using the two-step grid division algorithm model reported previously [34]. The allowable boundary error in this experiment was set as 0.5 mm. The point cloud resolution (ΔL) was 0.2 mm. The process of printing path planning cost about 3 s, and then the platform carried out printing according to trajectory. A dual-jet system was utilized to conduct bioprinting. once the dermis layer deposition finished, there was a pause in which another nozzle with epidermal bioink replaced automatically, and then the printing process continued.

2.6. Physical characterization of the 3D bioprinted constructs

To evaluate the mechanical properties, tensile tests were carried out for the printed constructs containing no cells at room temperature using an ETM103A electro-mechanical universal testing machine (WANCE, China) equipped with a 200 N load cell. The dimensions of the tensile samples are as shown in the Supplementary Fig. S1A-B. After applying a preload of 0.02 N, the tests were performed with a tensile rate of 10 mm/min until the samples broke, and the stress strain curves were recorded.

For degradation tests, 3D printed cell-free hydrogel constructs were immersed in PBS (pH = 7.4) at constant temperature (37 °C). Fresh PBS buffer was changed every 3 days. At the designated time points, the corresponding constructs samples were taken out and rinsed with DI water to remove excess salinity, and then they were dried in an oven at 60 °C for 48 h and weighed. The weight remaining ratio of constructs (%)

A

Samples	Gel (w/v)	Alg (w/v)	PRP (w/v)	TG (w/v)
AG-pre	10 %	4 %	0	0
AG	10 %	4 %	0	1 %
AG-2P	10 %	4 %	2 %	1 %
AG-5P	10 %	4 %	5 %	1 %
AG-10P	10 %	4 %	10 %	1 %

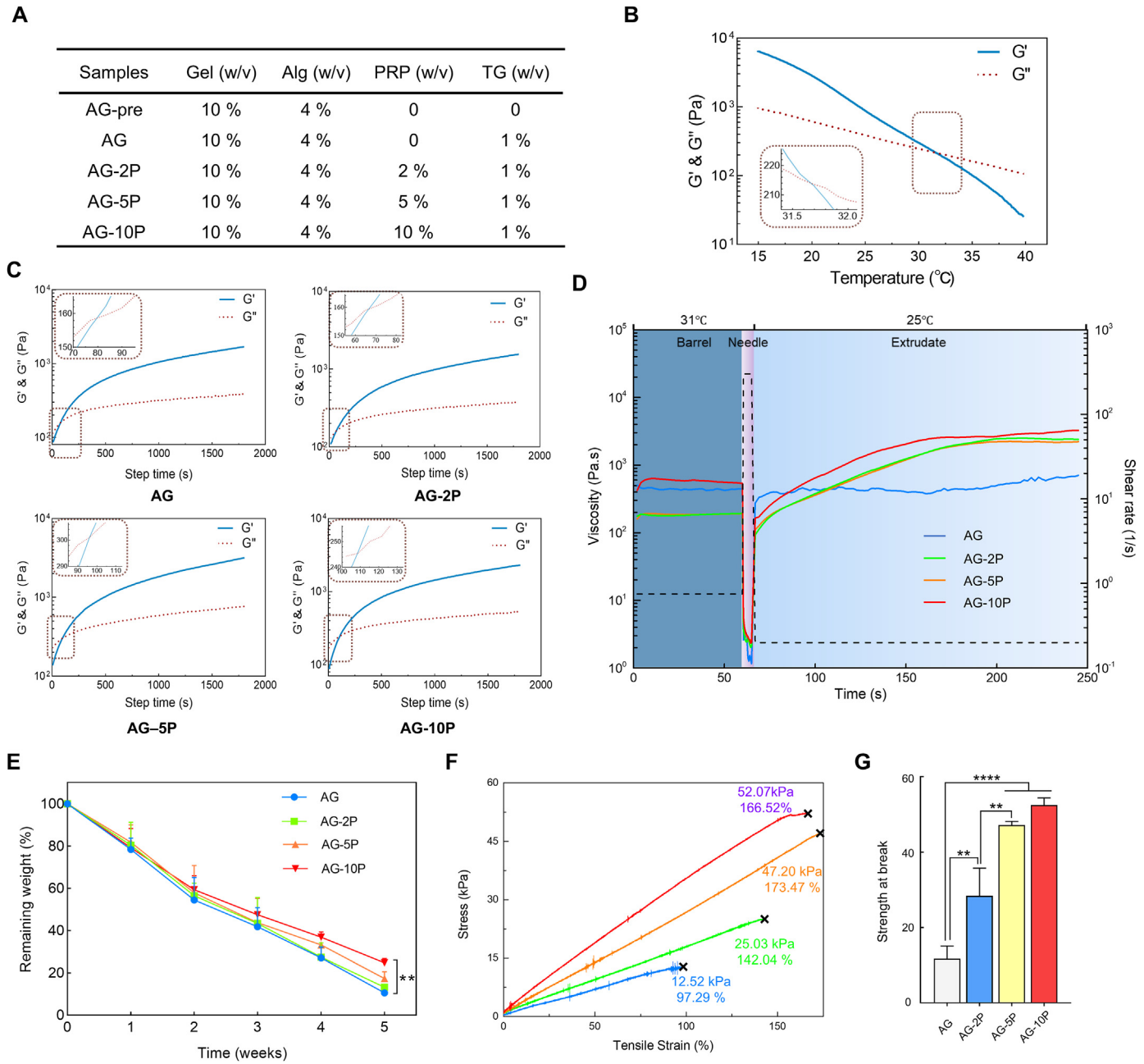

Fig. 4. General properties of bioink with PRP. (A) Components of hydrogel precursor samples. (B) Temperature sweeps of rheological tests on AG pre-hydrogel precursor. (C) The results of time-sweep oscillatory tests on hydrogels containing 0%, 2%, 5%, 10% PRP. (D) Peak hold tests exhibited sheer thinning and viscosity recovery during the extrusion printing process. (E) The degradation curves of cell-free 3D bioprinted constructs. (F–G) Stress-strain curves and statistical analysis of tensile tests. n = 3; $^{**}P < 0.01$; $^{****}P < 0.0001$ compared with the AG group.

$= (W_t\text{-}W_0)/W_0 \times 100\%$, where W_t and W_0 are the dry weight of the remaining constructs after degradation at different time points and the dry weight of initial constructs, respectively.

To conduct scanning electron microscope analysis, cell-embedded or cell-free construct patches were removed from culture medium after 1 week of culture. Specimens were washed in PBS for 3 times, fixed with 2.5% glutaraldehyde (Sigma-Aldrich, USA), dehydrated by vacuum freeze-drying for 48 h, sputter coated with gold (Hitachi, Japan), and examined with a field-emission scanning electron microscope (Hitachi, Japan) at 5 kV.

2.7. Assessment of biological effect on embedded seeded cells

2.7.1. Calcein-PI staining

A live/dead cell assay kit (Invitrogen, USA) was used to assess cell viability and morphology in the printed structure. The samples after culturing for 1, 4, and 7 days were submerged in dye solution composed of ethidium homodimer (EthD-4 μM) and calcein AM (2 μM) in 1 × PBS solution, followed by incubation at 37 °C for 30 min. A laser confocal microscope (Nikon, Japan) was utilized to capture Z-stack and projection images of the stained samples. The live cells appeared in green and the dead cells in red.

2.7.2. Cell proliferation, migration and toxicity detect

The CCK-8, scratch assay and lactose dehydrogenase (LDH) assays were performed as previously described [35]on HDFs and HESCs. 3D cell-printed construct patches were prepared with 100 μl cell-embedded bioinks as described above and incubated for various durations. The cell-free construct patches served as a blank control group. For scratch assay, cells were seeded onto a 24-well plate and incubated until they attained 80% confluence. A sterile 200 μl pipette tip was then used to scratch the cell monolayer. Next, we placed the upper chamber of transwell (Corning, USA) with 3D cell-printed construct patches of different PRP concentrations.

2.8. Function assessment of 3D printed HDFs-embedded dermal compartments

Total RNA was extracted using Trizol reagent (Invitrogen, USA) according to the manufacturer's instructions after 24 h and 48 h culture *in vitro*. The quality of obtained RNA was evaluated by the ratio of A260/A280. cDNA was synthesized with PrimeScript™ RT reagent Kit (Takara, Japan). RT-qPCR was performed with SYBR Green PCR Master Mix in the CFX Connect (BIO-RAD, USA), using GAPDH as internal control. The primers used were listed in Supplementary Table S1. Immunofluorescent staining and scanning electron microscope analysis was also performed as described in Part 2.11 and Part 2.6, respectively.

HESCs were seeded onto the printed HDFs-embedded dermal compartments and then cultured for up to 3 days. Cell filaments staining was implemented with phalloidin (30 μg/ml) in order to reflect the attachment and adhesion ability of epidermal cells on the surface of the 3D cell-printed dermal compartments.

2.9. Effect on other effector cells in wound healing

2.9.1. Enzyme-linked immunosorbent assay (ELISA)

The extract of 3D bioprinted hydrogel construct patches and the supernatant of Ca^{2+}-activated equal amount of PRP incubated for different durations at 37 °C were collected for growth factor assay by ELISA (Neobioscience, China) according to manufactures' instruction. For PRP activation, 10% (w/v) $CaCl_2$ was added to a final concentration of 1% within 5 min. PLTs released their therapeutic proteins into the surrounding plasma upon activation, and the fibrin clot was removed by centrifugation. The same amount of DPBS was used for the extraction of PRP-integrated patches or the dilution of PRP stock solution. Levels of platelet derived growth factor-bb (PDGF-BB) were detected.

2.9.2. In vitro biological effect on capillary formation and macrophage polarization

For transwell chemotaxis assays, 1×10^5 HUVECs were seeded onto the upper chamber of transwell 24-well plates (Corning, USA) with 8 μm pore filters. 3D bioprinted double-layered skin substitutes were prepared onto the lower chamber with 150 μL bioink. For the control and PRP group, 150 μL PBS or PRP was added instead. Similarly, 3D cell-printed double-layered skin substitutes of differ PRP concentrations were constructed into the upper chamber to stimulate the HUVECs seeded on Matrigel (Corning, USA) in the lower chamber. The Matrigel-based tube formation assay was performed as described above [36].

For the macrophage polarization assay, RAW264.7 cells were seeded on the 3D bioprinted double-layered skin substitutes. Lipopolysaccharides (LPS) (100 ng/ml) were added to the culture medium as a pro-inflammatory stimulation at the 8th hour. The expression of M1 marker (iNOS) and M2 marker (Arg-1) was determined by immunocytochemistry analysis.

2.10. Rat skin wound model and the wound area measurement

Healthy adult male Sprague-Dawley rats (220–250 g) were brought from Experimental Animal Centre of Air Force Military University. Anesthesia was induced with 5% isoflurane in oxygen and maintained at 2–4% during the surgery. The pelage on the rats' back was shaved, and the exposed skin was cleaned with povidone–iodine solution prior to the operation. The wound fixators (inner diameter of 20 mm) were pasted onto the surface of rats' dorsal skin with medical glue. Full-thickness excisional skin wounds (15 mm in diameter) was created. After the process of *in-situ* bioprinting, all the wounds were then covered by commercially available transparent film dressing (3 M, USA). Rats were housed individually post-operation with access to food and water ad libitum. The digital photographs were used to monitor the wound closure over time on days 0, 3, 7, 14 and 21 post surgery. Then, the wound area was determined by tracing the wound margins with ImageJ software [37]. Rats were sacrificed and their dorsal skin was surgically removed for histological analysis.

2.11. Histological analysis and immunofluorescence staining

HE, Masson's trichrome and Picrosirius red staining were carried out as previously described [38]. Collagen were stained blue in the Masson staining. Picrosirius red staining was used to detect the distribution of different collagen types with polarized light microscopy. Images were taken for 1-week and 3-week specimen, which represented the collagen synthesis in the early and late stages of wound repair. Besides, immunostainings were carried out for collagen I (COL-1; Abcam, UK), collagen III (COL-3; Abcam, UK), CD31 (Abcam, UK), α-SMA (Abcam, UK), CD68 (Servicebio, China), CD3 (Servicebio, China), Fibrinogen (ThermoFisher Scientific, USA), Decorin (DCN; Abcam, UK), Fibronectin (FN; Servicebio, China), Myeloperoxidase (MPO; Servicebio, China), iNOS (Abcam, UK) and Arg-1 (Abcam, UK) according to the provider's instructions. Images were taken under an FSX100 microscope (Olympus, Japan). Integrated fluorescence intensity was measured from three random figures in one group by integrated grey value from ImageJ.

2.12. Blood perfusion assessment with Doppler detection

The blood flow of the wounds was assessed with a laser Doppler perfusion imaging (LDPI) analyzer (PeriMed, Sweden) on day 14 post surgery. Briefly, the rats were anesthetized with isoflurane. The mean blood perfusion was detected in the wound area of rats (ROI 1) as well as the surrounding skin at a standard distance from the wound border (ROI 2). The mean perfusion ratio was counted by comparing the ROI 1 value with the ROI 2 value.

2.13. Statistical analysis

All experimental data were obtained from at least three independent experiments and analyzed as the mean ± standard error (SEM). The comparisons between two groups were analyzed using Student's *t*-test, and the comparisons among multiple groups were conducted using analysis of variance followed by Turkey's post hoc test. A value of $P < 0.05$ was considered statistically significant.

3. Results and discussion

3.1. PRP preparation and the integration into alginate sodium-gelatin hydrogel

Human and rat PRP was prepared by twice gradient centrifugation successfully. we demonstrated the enrichment of PLTs (6.6 times for human and 5.2 times for rat) and white blood cells (WBCs; 2.9 times for human and 4.3 times for rat) by the current preparation method using blood cell count (Fig. 3A), which met the preparation standards of PRP [21,39].

To observe the internal morphology of hydrogels AG, PRP and AG-10P, cell-free samples were prepared and observed with scanning electron microscope. Among them, the PRP gel was prepared via the crosslink

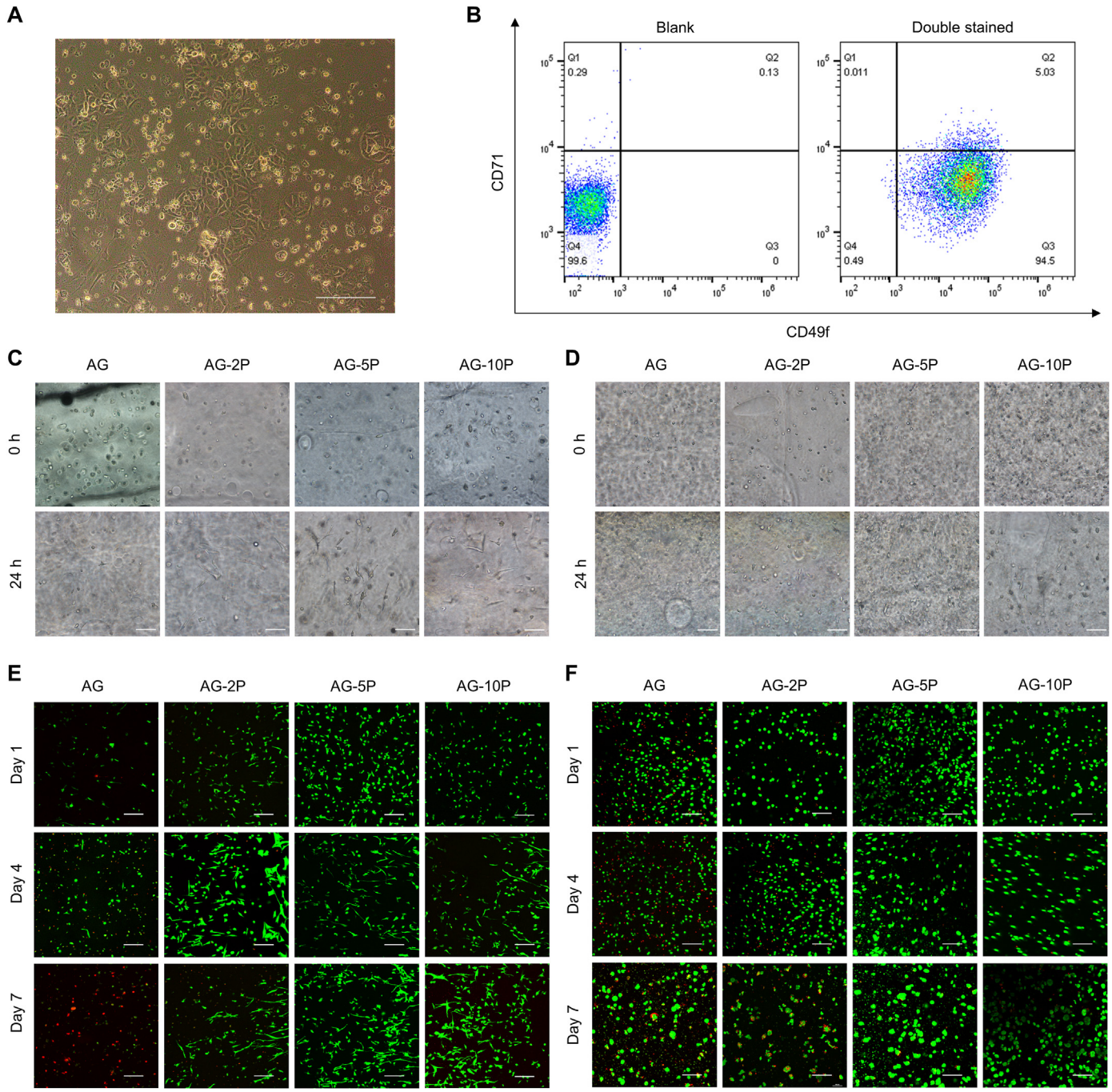

Fig. 5. Viability of seeded cells within 3D bioprinted constructs. (A–B) Isolation and identification of primary ESCs identification. (C–D) Brightfield imaging of embedded HDFs (C) and HESCs (D). (E–F) Confocal imaging after Calcein-PI staining of embedded HDFs (E) and HESCs (F). Scale bar: 200 μm.

of PRP by 1% (w/v) calcium chloride for 15 min. It could be demonstrated that PRP gel exhibits a denser fiber network structure and smaller pores compared with AG. In the AG-10P composite hydrogel, the fibrin component of PRP was integrated into the main network of gelatin, reducing the pore size and introducing sites for cell adhesion. Masson's trichrome staining (MTS) confirmed the difference in porosity between AG and PRP gel, as well as the integration of their matrix components in the composite gel. The mouse monoclonal anti-fibrinogen antibody (ThermoFisher Scientific, USA) was applied to reveal the distribution of PRP components inside by immunofluorescence detection, and it was found that it was uniformly dispersed (Fig. 3C). Actually, autologous PLTs- and plasma-derived fibrin scaffolds has been emerging as a safe and efficacious natural system to repair musculoskeletal tissues and corneal ulcers [40].

Excellent hemocompatibility is an essential attribute of scaffold implants or wound dressings. To evaluate whether the bioinks were compatible with blood, the *in vitro* direct contact hemolytic activity was calculated by the supernatant absorbance detection. As shown in Fig. 3B, the hemolysis ratios of all bioinks were lower than 2%, indicating sufficient hemocompatibility and systemic safety.

PRP has been served as a promising alternative for protein therapies to improve clinical outcomes in the field of tissue regeneration [41]. These proteins, particularly growth factors and cytokines, mediate communication between cells or between cells and ECM environment.

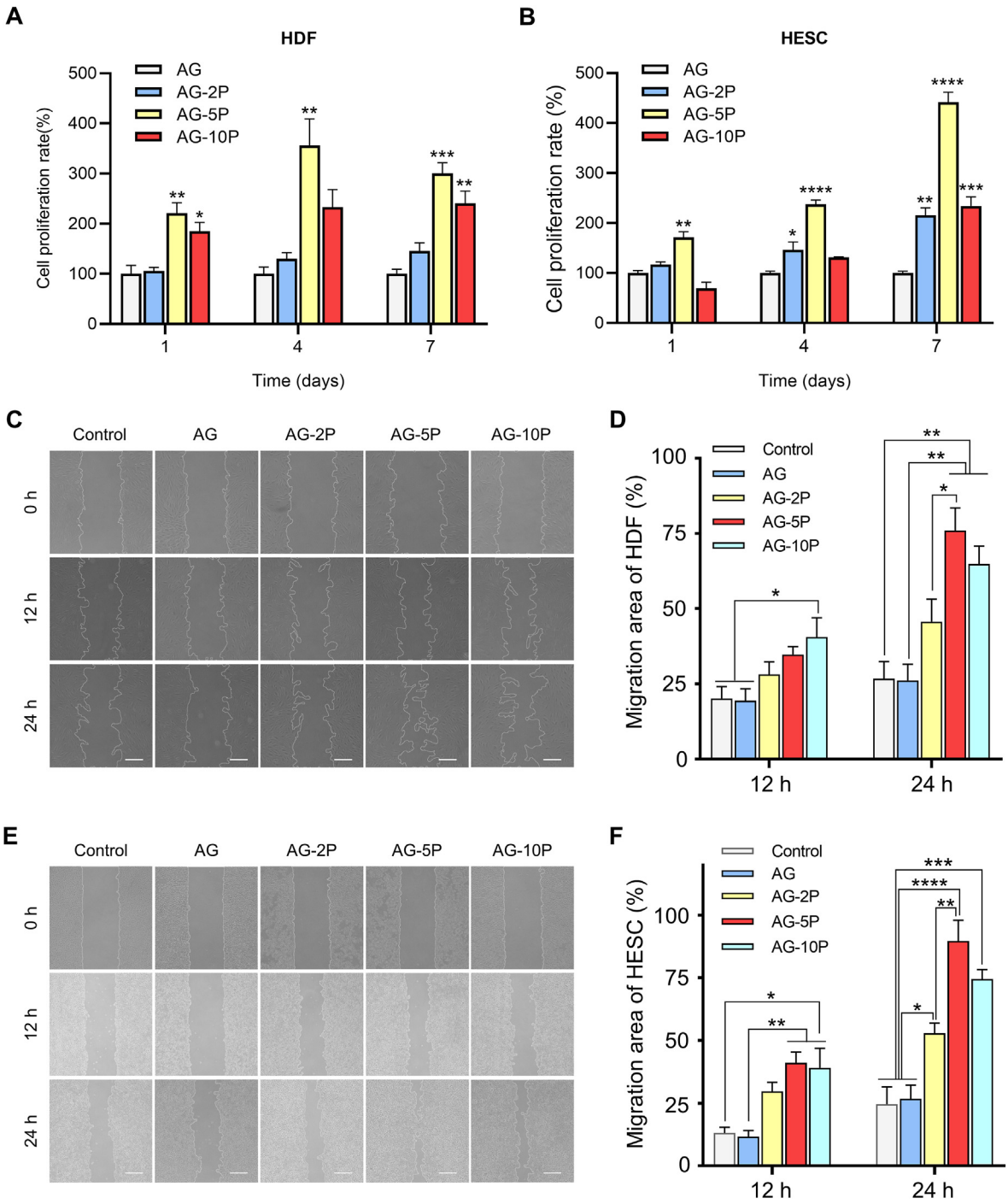

Fig. 6. Proliferation and migration of seeded cells within 3D bioprinted constructs. (A–B) CCK-8 assay for the proliferation of embedded HDFs (A) and HESCs (B). (C–F) Scratch assay for the migration of HDFs (C–D) and HESCs (E–F). Scale bar: 100 μm; Data are expressed as the mean ± SEM; n = 3; *$P < 0.05$; **$P < 0.01$; ***$P < 0.001$; ****$P < 0.0001$.

When incorporated into bioinks, it may have the potential to protect seeded cells during extrusion, provide biological cues for them and injured tissues to accelerate healing and maturation of bioprinted skin substitutes. Previous studies often focused on grafting a specific growth factor with biomaterials. The procedures were cumbersome and the introduction of chemical substances would cause toxic reactions [42]. The synergy between the various growth factors of PRP could simplify the integration process. It's reported that the activated PRP gel alone degrades rapidly with short-term bioactive effects [43], while the integration of PRP into AG bioink is hypothesized to prolong the release of bioactive factors that are beneficial to tissue regeneration.

3.2. Rheological properties of PRP composite bioinks and bioprinting parameters determination

In order to improve the precision of extrusion printing in the biomanufacturing process, rheological tests were performed to determine the condition parameters for bioprinting to obtain the best extrusion effect suitable for the specific bioinks. For temperature selection, the results of temperature sweep test revealed that the storage modulus (G′) of Sample AG-pre was equal to the loss modulus (G″) at 31.7 °C (Fig. 4B), which was the gel temperature. When the temperature was higher than it, the pre-hydrogel sample was fluid, otherwise it's gelatinous. It's mainly

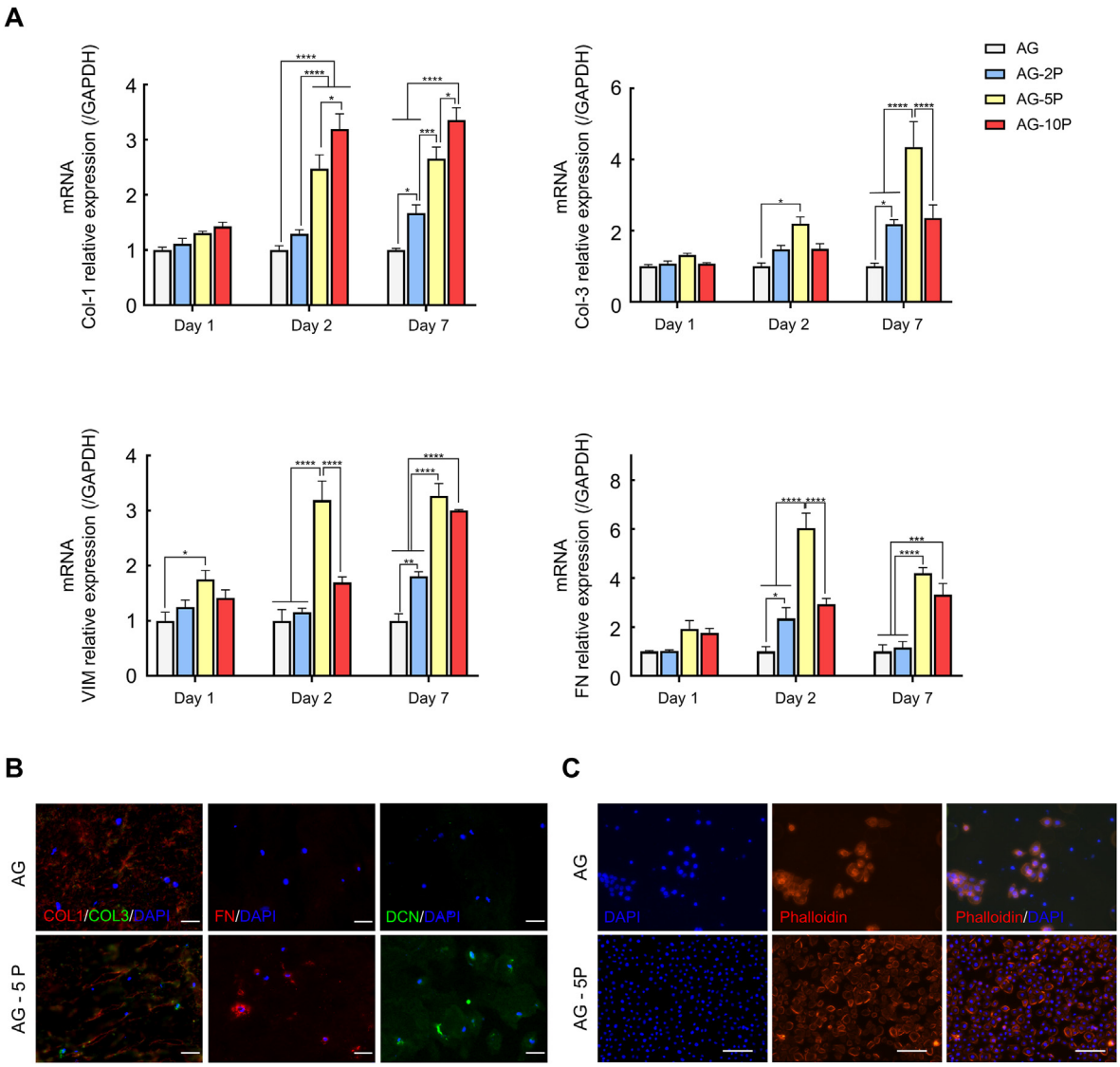

Fig. 7. Functional evaluation of 3D bioprinted dermal compartments (A) RT-qPCR test for the 3D printed dermal compartments; Data are expressed as the mean ± SEM; n = 3; $*P < 0.05$; $**P < 0.01$; $***P < 0.001$; $****P < 0.0001$. (B) Immunofluorescent staining for the 3D printed dermal compartments. Scale bar: 30 μm; (C) Phalloidin staining for the cell adhesion of HESCs on 3D printed dermal compartments. Scale bar: 100 μm.

related to the phase change characteristics of gelatin with temperature [44]. Therefore, combined with the actual extrusion effect, we set the printing temperature of the nozzles to 31 °C by the temperature control element. At this temperature, the storage modulus of AG composite was slightly higher than the loss modulus and it exhibited a solid-liquid coexistence state.

The curves of G′ and G″ of Sample AG, AG-2P, AG-5P, and AG-10P containing the enzymatic crosslinker were recorded over time to analyze the influence of different PRP concentrations on the printability of bioinks. As shown in Fig. 4C, the AG-PRPs were rapidly gelled when the G′ surpassed the G″ within 79, 67, 96 and 108 s for 0, 2%, 5% and 10% PRP. It seemed that the gelation time increased with the concentration of PRP, but the differences between the concentration groups were small. Similarly, the viscosity decreased with the increase of shear stress in all groups (Supplementary Fig. S2). The sheer thinning characteristic would be beneficial to protect the seeded cells encapsulated in bioinks from injury during the extrusion process [45]. Moreover, peak hold tests revealed a rapid shear recovery following dramatic shear thinning, during which the change of mechanics experienced by the bioinks during bioprinting process were closely mimicked (Fig. 4D). Therefore, the incorporation of PRP did not show significant impact on rheological properties and printability of the bioinks.

3.3. Physical assessment of the cell-free printed constructs

Since the prepared bioink was to be utilized for *in-situ* printing construction research, it needs to have more stable physical properties after deposition and crosslink than ordinary bioprinting [9]. We tested the degradative and mechanical properties of the cell-free printed constructs with different PRP concentrations.

The degradation curves were plotted and revealed that all groups were biodegradable, and the degraded mass increased with the immersion time (Fig. 4E). As shown in the figure, after immersed in PBS at 37 °C for 5 weeks, the AG group degraded the fastest and the remaining mass percentage was 10.61 ± 1.24%. With the increase of PRP concentration, the remaining mass percentages increased to 13.21 ± 1.57%, 17.33 ± 3.22% and 24.75 ± 2.06% for groups of AG- 2, 5, 10 PRP, respectively. In other words, the groups with higher PRP concentration degraded slightly more slowly than that with lower PRP concentration, which may be due to the crosslinking of the fibrinogen component of PRP and the formation

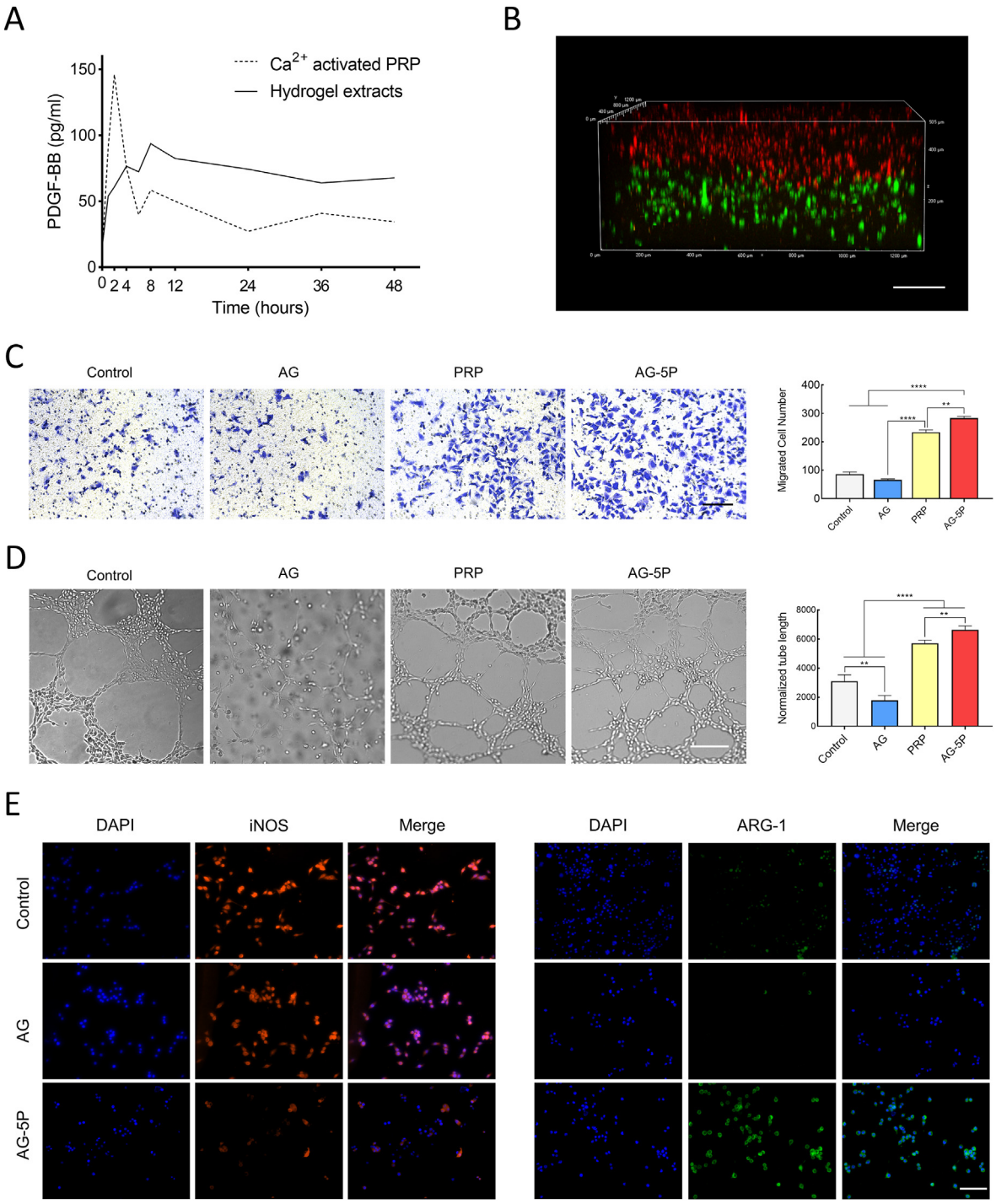

Fig. 8. The effect of 3D bioprinted double-layered skin substitutes on HUVECs and macrophages (A) ELISA results of PDGF-BB release. (B) The laser confocal micrograph of an *in vitro* 3D bioprinted double-layered substitute. Scale bar: 200 μm. (C) Transwell migration assay of HUVECs co-cultured with 3D bioprinted substitutes. Scale bar: 100 μm. (D)Tube formation assay of HUVECs co-cultured with 3D bioprinted substitutes. Scale bar: 200 μm. (E) Immunofluorescent staining of Raw 264.7 macrophages co-cultured with 3D bioprinted substitutes. Scale bar: 200 μm. Data are expressed as the mean ± SEM; n = 3; $^{**}P < 0.01$; $^{****}P < 0.0001$.

of fibrin networks within the constructs. However, with the exception of the AG and AG-10P groups at the 5th week, there was no statistical difference between the remaining mass percentages at each time point and each group. The degradation of a bioink could enable more cell exchange between the *in-situ* autologous tissue and the printed constructs, so the seeded cells or bioactive molecules could be accurately delivered to the wound bed. Correspondingly, local resident cells could also infiltrate into the biomaterial to realize the gradual transform and functionalization of the microenvironment into a regenerated niche [46]. It's also reported that less degradation may be more conducive to the application in chronic difficult-to-heal wounds such as diabetic wounds [47].

The elasticity and stiffness of artificial skin are of great importance to the wound healing [48], and the mechanical properties of the 3D cell printing bioinks after gelation would affect the mechanical stress on seeded cells and their biological behavior [49]. Stress-strain curves of printed cell-free specimens with AG-PRPs were presented in Fig. 4F. The tensile strength at break of the cell-free constructs increased with the increase of the PRP concentration in the bioinks, which may be attributed

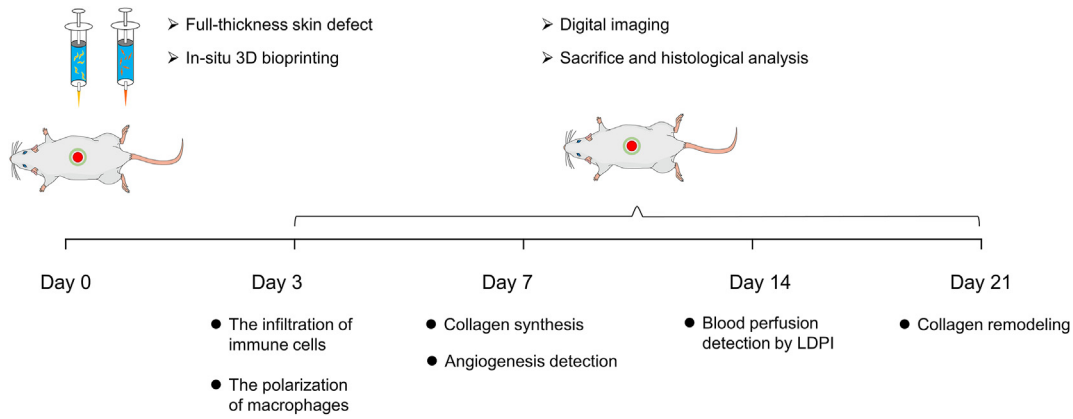

Fig. 9. The schematic illustration of the animal experimental process which includes the observation items at each time point.

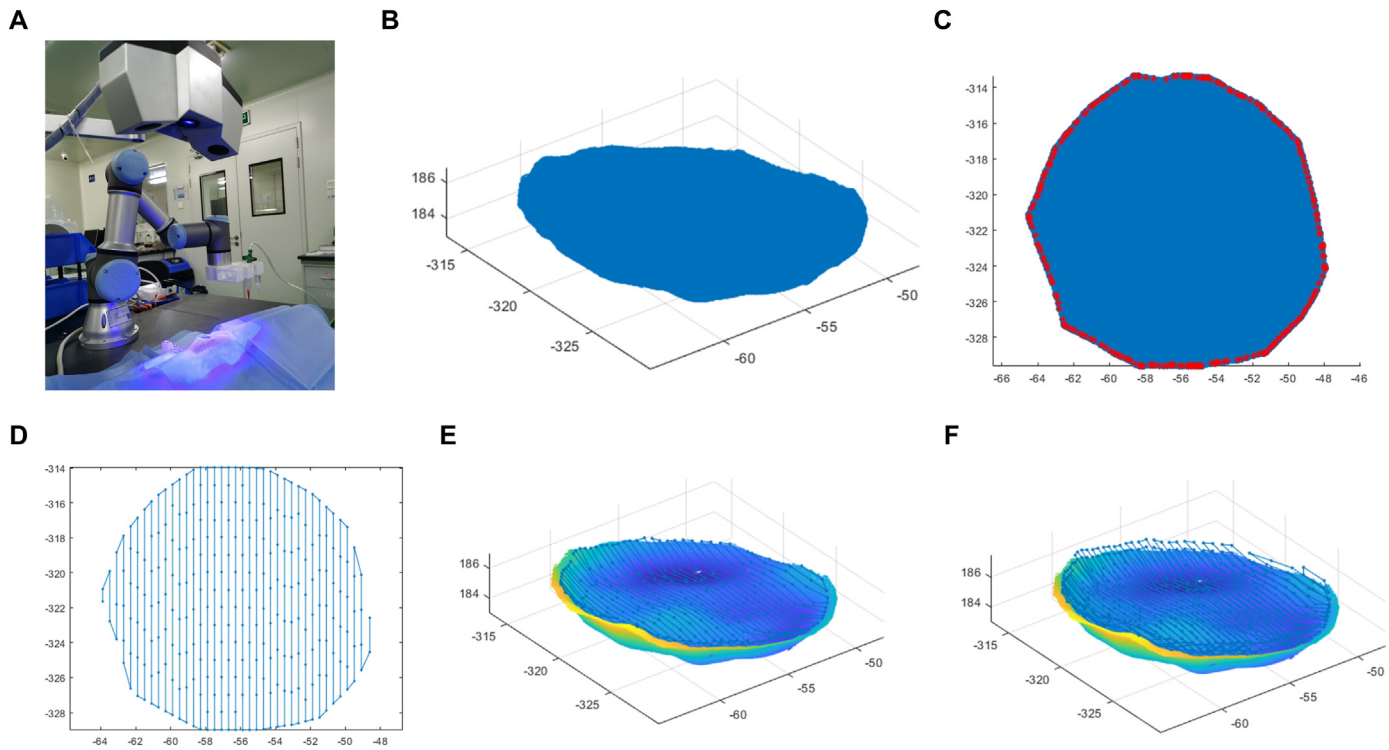

Fig. 10. Wound scanning and Path planning sequence for the point cloud according to the defect. (A) The skin defect was scanned using a binocular optical 3D scanner. (B) the point cloud of the bottom surface of the skin defect site obtained with existing programs. (C) A single-layer point cloud was projected on a 2D plane and the contour point was marked by asterisks. (D) A 2D printing path was generated. (E–F) Two layers of 3D printing paths were generated. Scale bar units: mm (B–F).

to the intramolecular hydrogen bonding of fibrin produced by the crosslinked PRP in the constructs. It indicated that the integration of PRP could improve the overall mechanical properties of bioink materials after crosslinking. It's worth emphasizing that these values were derived from samples without cells. Seed cells could also secrete ECM in a suitable artificial matrix to further improve the overall mechanical properties of the constructs [37]. Previous studies have also shown that the fibrinogen component in PRP can increase the affinity of collagen-based hydrogel scaffolds for fibroblasts and keratinocytes [50]. We would also study the influence on the seeded cell behavior next.

3.4. The effect of PRP-integrated 3D bioprinted constructs on the viability, proliferation and migration of seeded cells in vitro

Human and rat-derived DFs and ESCs were successfully isolated. It was observed that isolated ESCs were regular polygons like paving stones, and the cell volume was small, the nucleus was relatively large with a stereoscopic vision under the microscope (Fig. 5A). According to flow cytometry identification, the CD71(−)/CD49f (+) HESCs accounted for 94.5% (Fig. 5B).

Cellular behaviors, for instance, cell adhesion, extension, proliferation and migration, are regarded as crucial indicators for 3D *in vitro*

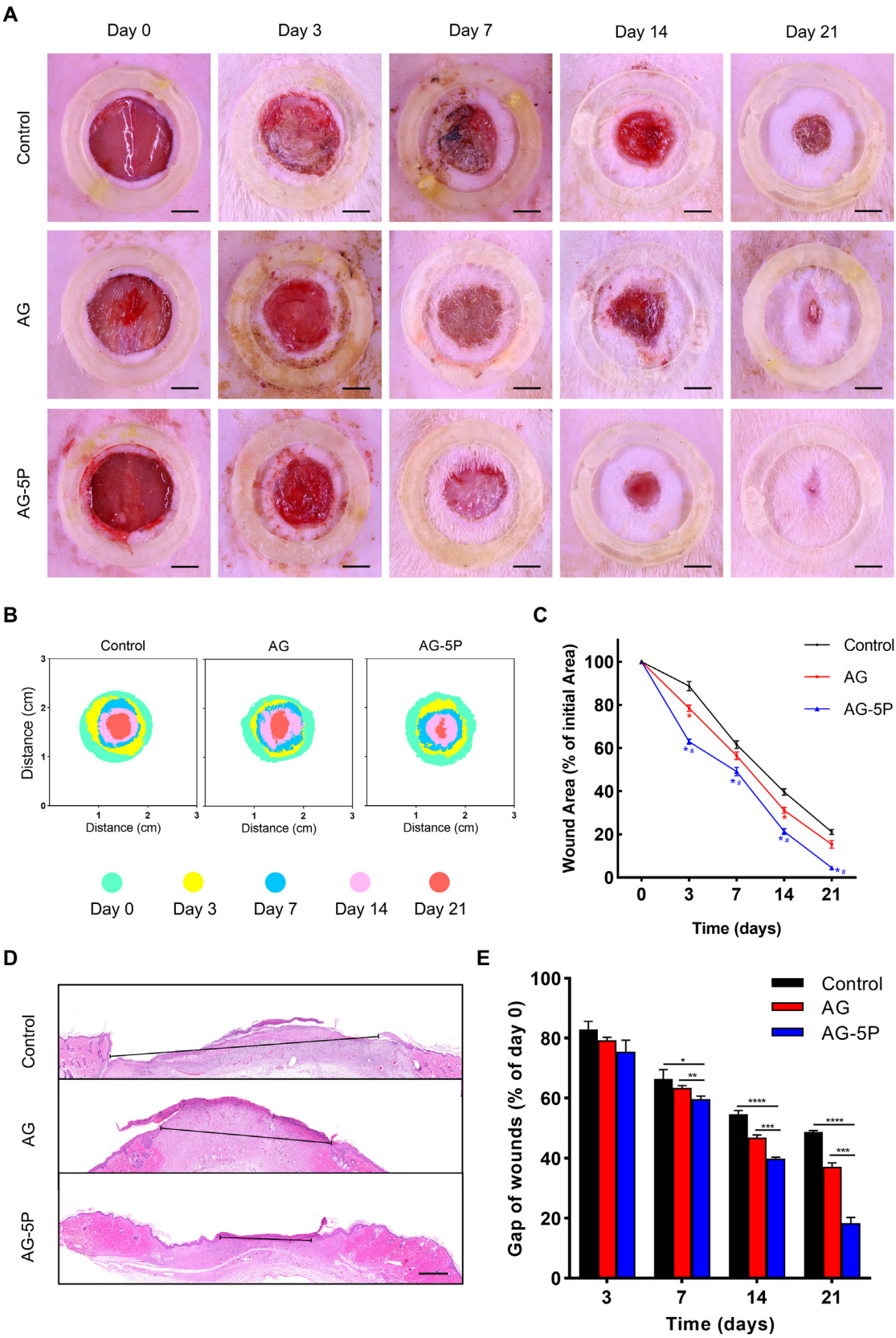

Fig. 11. The wound closure in rat model after *in-situ* bioprinting. (A–C) The wound closure rate within 21 days after *in-situ* bioprinting. Scale bar: 5 mm; $*P < 0.05$ compared with Control group; $\#P < 0.05$ compared with AG group. (D–E) Typical photographs of HE staining for the wound on day 21 (D) and quantitative results within 21 days (E). Scale bar: 500 μm. Data are expressed as the mean ± SEM; n = 3; $*P < 0.05$; $**P < 0.01$; $***P < 0.001$; $****P < 0.0001$.

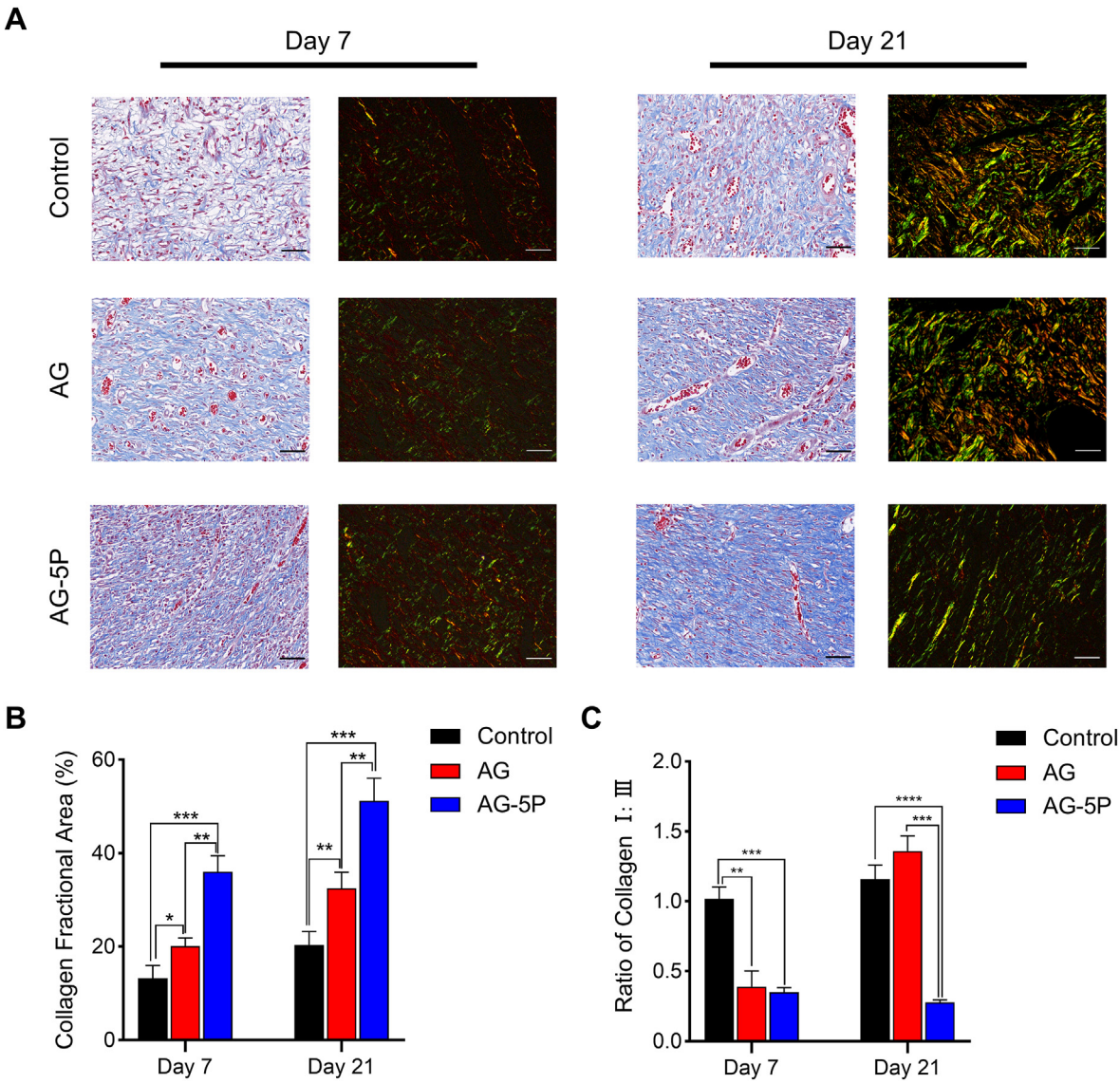

Fig. 12. Masson and Picrosirius red staining for determination of collagen synthesis in rat model on day 7 and day 21 after *in-situ* bioprinting. (A) Typical photographs of MTS and Picrosirius red staining at Day 7 and 21 of all the groups. Scale bar: 50 μm. (B) The quantitative results of MTS on collagen deposition. (C) The quantitative results of Picrosirius red staining on the ratio of COL I/III. Data are expressed as the mean ± SEM; n = 3; $^{*}P < 0.05$; $^{**}P < 0.01$; $^{***}P < 0.001$; $^{****}P < 0.0001$.

culture models [46]. Under the bright field microscope, the seeded cells in each PRP concentration group showed a spherical shape immediately after the bioprinting was completed. After 24 h of culture, the cell morphology spread to varying degrees (Fig. 5C and D). After 1, 4 and 7 days, cell viability of laded HESCs and HDFs in the 3D printed constructs was analyzed by Calcein-PI staining (Fig. 5E and F). Compared with other groups, HDFs and HESCs observed in the constructs of the AG-5P group had fewer dead cells. Cell activity on day 1 was more related to printing parameters, owing to shear stresses inflicted on cells in non-Newtonian fluids and hypoxia [18]. The results revealed that the integration of PRP could neutralize some of the adverse environmental stimuli related to printing, which is critical in future *in vivo in-situ* applications, because it could increase the initial colonization rate of seeded cells on the wound. On day 4 and 7, the PRP-integrated groups still maintained a higher cell survival rate. Fully spread cell morphology could be observed, which facilitated performing the physiology functions in the matrix. Therefore, the AG-PRPs composite bioinks could provide a more favorable cell growth environment for HDFs and HESCs, and provide rich nutrition and space for cell growth and survival, and furthermore, 5% may be the best PRP concentration.

The selection of the optimal concentration of PRP in tissue repair and regeneration applications has also attracted attention in other studies. Recent studies showed that the integration of 20% PRP into the hydrogel showed optimal effects on the osteogenic and chondrogenic differentiation of BMSCs [43]. For *in-situ* bioprinting, as the provider of initial signal for repair and regeneration [51], the selection of PRP concentration in the bioink is of great importance. It affects the interaction between artificial substitutes and the wound beds, as well as the viability and functioning of seeded cells. Cell proliferation was evaluated by CCK-8 assay, and the results were shown in Fig. 6A and B. On day 7, constructs supplemented with AG-2P, AG-5P and AG-10P exhibited better cell proliferation than pure AG bioink. Among them, the pro-proliferation effect of AG-5P was the most prominent. This conclusion was consistent with the results of Calcein-PI staining. The HDFs proliferated tardily for the PRP-integrated groups from the day 7–14, probably due to the saturated spread of cells within the internal microporous environment. The results of scratch wound assays showed that the incorporation of PRP markedly enhanced the motility of HDFs and HESCs, as determined by the migration area (Fig. 6C–F, Supplementary Fig. S3). After 24 h, the migration rate of HDFs in the AG-5P and AG-10P groups significantly

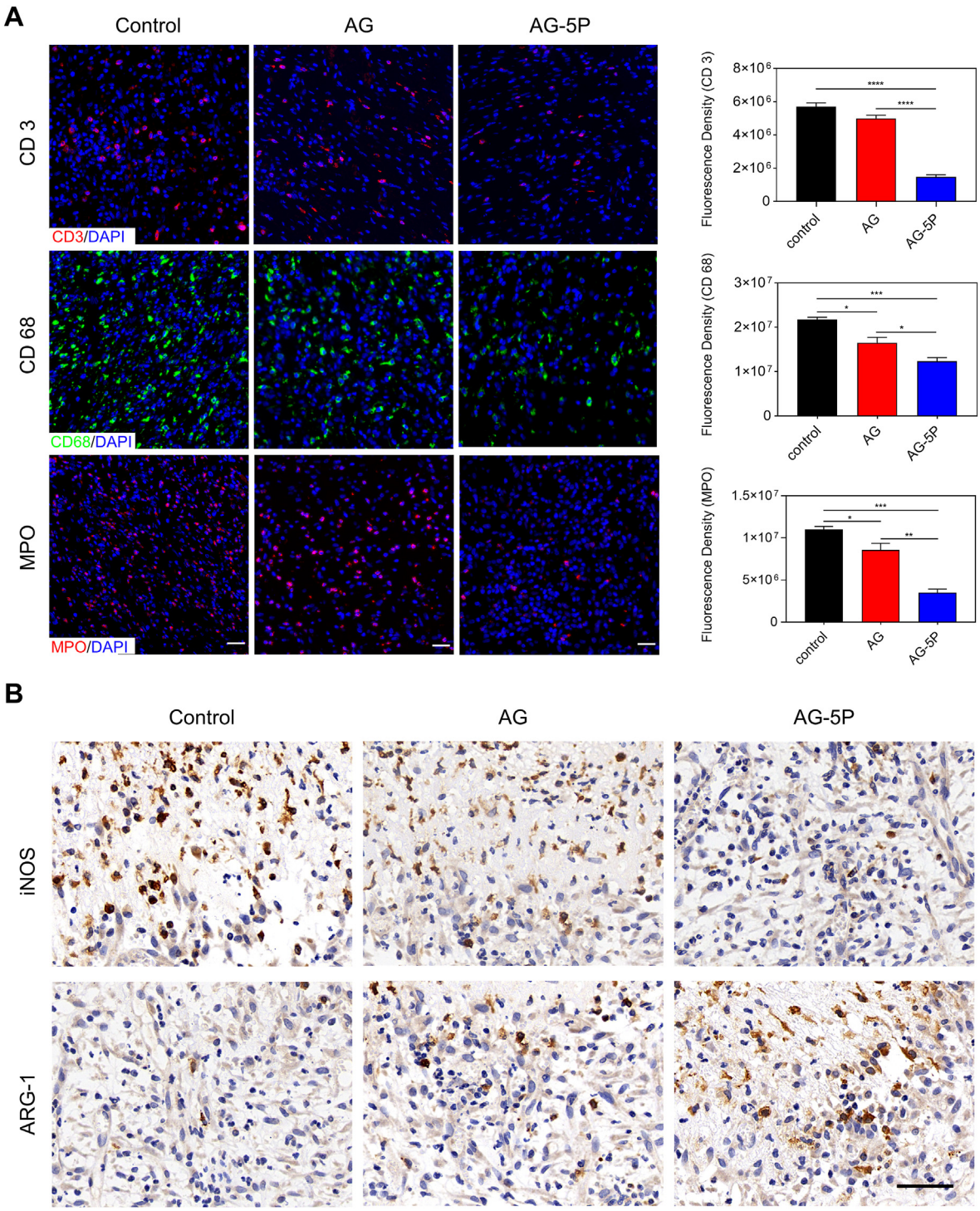

Fig. 13. The inflammatory cell infiltration in rat model on day 3 after *in-situ* bioprinting (A) Immunofluorescent staining for infiltrating inflammatory cells. Scale bar: 30 μm; Data are expressed as the mean ± SEM; n = 3; *$P < 0.05$; **$P < 0.01$; ***$P < 0.001$; ****$P < 0.0001$. (B) Immunohistochemical staining of iNOS and ARG-1 to determine the polarization of macrophages on day 3. Scale bar: 50 μm.

exceeded the AG. Three groups of AG-PRPs all showed a significant promotion effect on the migration of HESCs. Fibroblasts are the major effector cells in the repair of soft tissue, during which a tissue-scale coordination is driven by the collaboration of fibroblast lineages proliferation, migration and ECM deposition, which may be essential to achieve a homeostatic substitute architecture during wound healing [29,52].

3.5. Function assessment of 3D printed HDFs-embedded dermal compartments

The dermis is an important part of the skin and closely related to the elasticity, abrasion resistance, function and appearance after wound healing [53]. In the treatment of burn wounds, thin split thickness skin

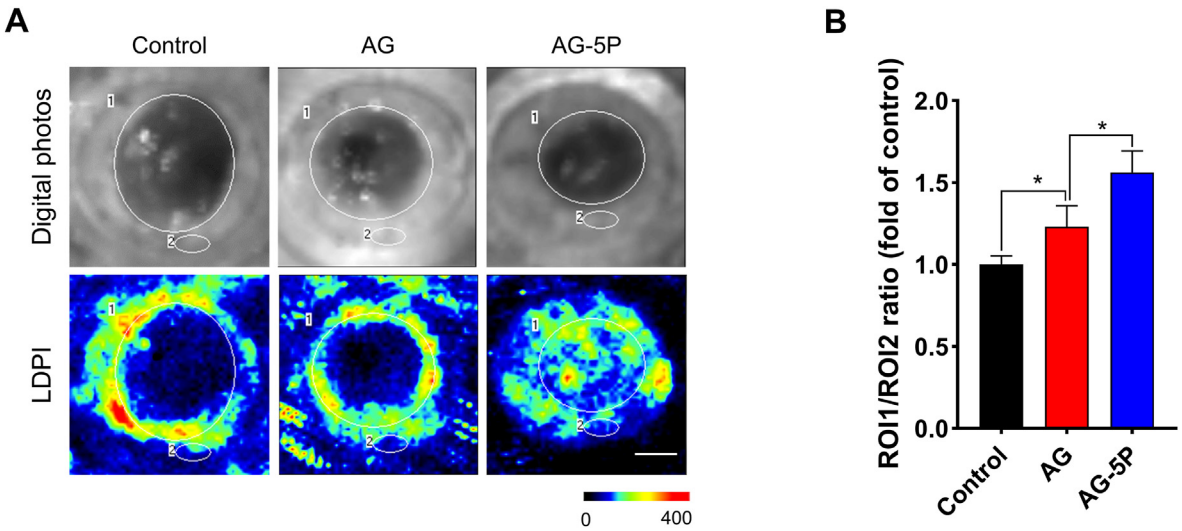

Fig. 14. LDPI to detect the blood perfusion into *in-situ* bioprinted substitutes on day 14 (red and yellow regions indicate high perfusion, blue and dark blue regions indicate low and no perfusion, respectively). Scale bar: 500 μm; Data are expressed as the mean ± SEM; n = 3; $^*P < 0.05$.

graft lacking dermal structure is often accompanied by local scar hyperplasia, blistering and ulcerating or even dysfunction [54]. In order to improve the quality of wound healing, dermal substitutes or scaffolds have become a hot spot in skin tissue engineering research [42]. Therefore, the dermal compartment of the 3D bioprinted skin substitutes ought to be preeminent and stable in structure and function to ensure the overall repair effect.

To determine gene transcription profiles of HDFs laded in 3D printed dermal compartments *in vitro*, RT-qPCR was performed to detect the COL-1, COL-3, FN and Vimentin (VIM) to compare the relative mRNA levels of the cells embedded in AG and AG-PRPs for 1, 4 and 7 days after normalizing with glyceraldehyde 3-phosphate dehydrogenase (GAPDH; Fig. 7A). The expression of the COL-3, FN, and VIM were significantly upregulated in AG-5P over another groups, throughout the culture periods. However, for COL-1, the expression level of AG-10P group was the highest. The immunofluorescent staining for 3D printed artificial dermis layer cultured for 7 days *in vitro* also reached similar conclusions. Specific staining was performed for secreted ECMs, including COL-1, COL-3, DCN and FN, which constituted the main components of native skin ECM. By comparing the fluorescence intensity of AG-5P and AG group, it could be observed that the integration of PRP makes HDFs secrete ECM significantly higher than the control group (Fig. 7B). For the double staining of COL-1 and COL-3, it's noteworthy that the fibroblasts encapsulated in the AG-5P group secreted more COL-3, resulting in a decrease in the ratio of COL-1: COL-3.

COL-1 is the predominant collagen type synthesized mainly by fibroblasts. The coordination of its synthesis and degradation often determines the speed and quality of wound healing, as well as whether the excessive fibrosis of cutaneous scars could happen [55]. FN could serve as a biological glue mediating the interaction between cells and other ECM protein, and pre-coating the wound bed with FN could significantly improve the local utilization and function of exogenous ESCs. VIM constitutes a major portion of the cytoskeleton of fibroblast. Upregulation of COL-3 relative to COL-1 ratio deposited at wound sites is regarded as a biological signal of high-quality repair, such as scarless healing and fetal regenerative repair process [56]. Therefore, the seeded cells for *in-situ* skin bioprinting need to rapidly initiate the paracrine process of the above-mentioned molecules after being embedded into the local biological niche of the biomaterial matrix, thereby forming an ideal microenvironment for cell adhesion and migration not only inside the skin substitute, but also at the interface with autologous tissue, to initiate maturation of the substitute as well as infiltration of autologous cells.

In order to detect the adhesion of HESCs after seeding on the surface of the HDFs-embedded dermal compartment with or without PRP, DAPI and phalloidin staining were performed (Fig. 7C). It was observed that the number of HESCs adhering on the surface of AG-5P group was significantly higher than AG group, and the cell morphology exhibited a typical paving stone appearance, indicating the promotion of initial cellular attachment. Furthermore, there were cell patchy colonies formation in AG group, while the AG-5P group showed an almost monolayer fusion distribution. The former is not conducive to the differentiation and maturation of the epidermal layer and tends to peel off from the basal substrate. It indicates that PRP in the dermal compartment can improve the cell behavior of epidermal cells on it, which may also be related to the secretion of the aforementioned matrix by the embedded HDFs.

3.6. The sustained release of PRP-derived growth factors from 3D printed skin substitute and the effect on vascular endothelial cell and macrophage

The concentration of PDGF-BB in the surrounding liquid of PRP-integrated 3D printed hydrogel was analyzed by ELISA at different time points and compared with an equal amount of PRP directly activated by calcium ions. PDGF-BB is one of the most abundant growth factors in PRP, and it's approved by the U.S. FDA for the treatment of diabetic foot ulcers for the efficacy and high safety. As shown in Fig. 8A, the Ca^{2+}-activated group exhibited an initial burst release, while the AG-PRP group exhibited a 50% burst release from the constructs within 4 h and then levelled off. It's the loose and porous structure inside the printed constructs that allowed the PRP component to reside and stably escape. Other attempts that incorporated PRP into hydrogels to prolong the release of bioactive factors have been made in different applications [57]. Therefore, we explored whether the skin substitute could affect the cell behavior of not only the encapsulated seeded cells, but also the autologous cells at the wound bed, such as vascular endothelial cells and inflammatory cells. Next, we would stimulate these cell types by co-culturing with 3D printed double-layered artificial skin substitutes (Fig. 8B) to test the effect on recruited effector cells.

It is well established that rapid angiogenesis is a key factor in the functionalization of artificial skin substitutes and wound healing [58], in which the vascular endothelial cells of the wound bed act as the main effector cells. Hence, we performed co-culture experiments to test the effect of PRP-embedded substitutes on biological functions of HUVEC. The results of transwell migration assay revealed that the HUVEC migration of AG group was slightly lower than control group. The

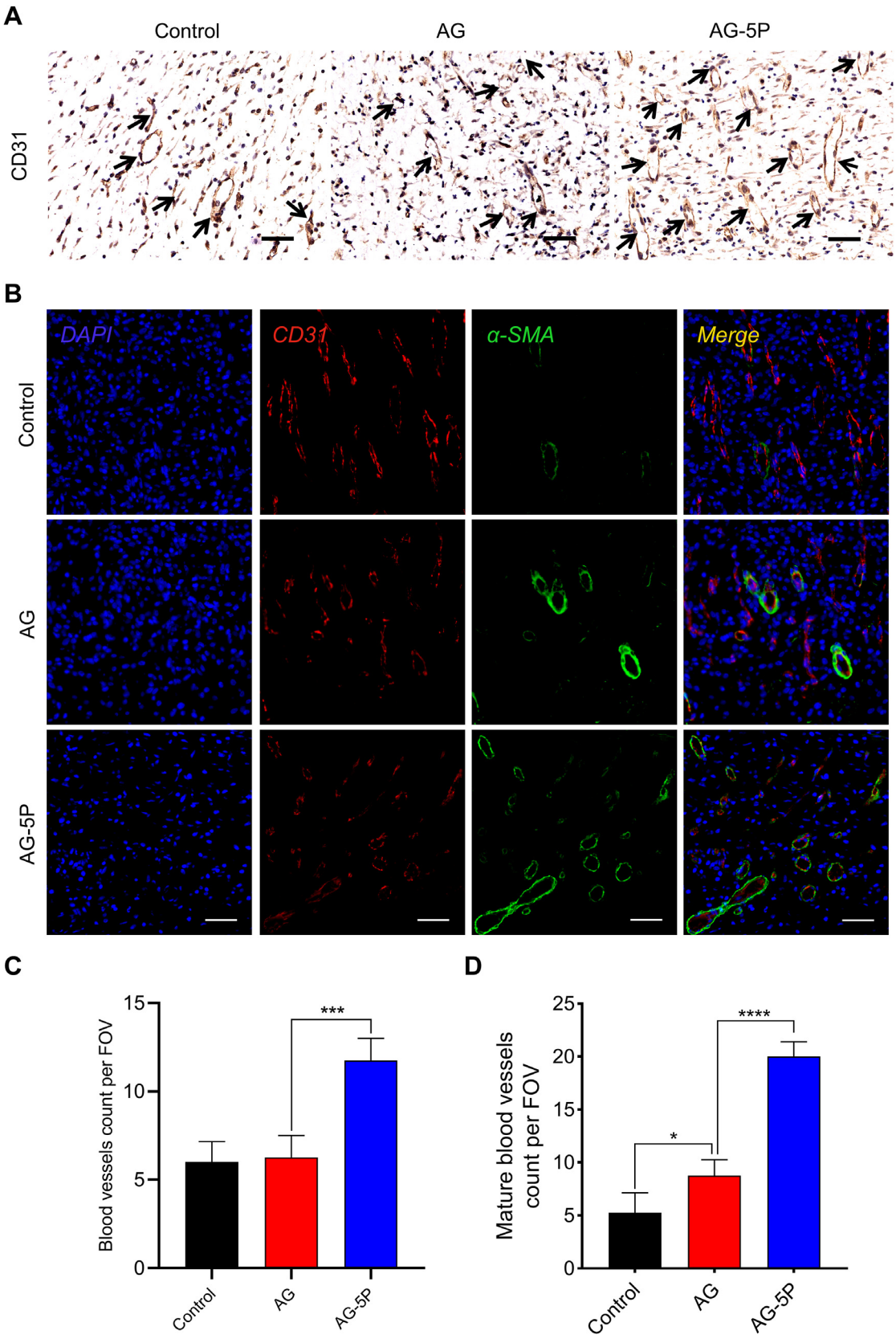

Fig. 15. Evaluation of *in vivo* angiogenesis in the *in-situ* bioprinted constructs on day 7. (A, C) IHC staining of CD31 and the quantitative results. Scale bar: 50 μm. (B, D) Immunofluorescent staining of CD31 and α-SMA for mature blood vessels. Scale bar: 50 μm. Data are expressed as the mean ± SEM; n = 3; $^{*}P < 0.05$; $^{***}P < 0.001$; $^{****}P < 0.0001$.

Table 1
The values of bioprinting parameter settings in extrusion-based bioprinting for *in vitro* culture, as well as for *in-situ in vivo* rat full-thickness cutaneous defect repair.

Parameter		Value
Extrusion pressure (MPa)		0.15
Nozzle diameter (μm)		200
Printing speed (mm/s)		15
Printing temperature (°C)		31
Distance between nozzle to substrate (mm)		1
Fabrication dimension (cm^3)	*In vitro* bioprinting	15 × 15 × 0.3
	In-situ in vivo bioprinting	Scanned topography

integration of PRP in the AG reversed this effect, and the migrated cells were more than the group directly applied with an equal amount of PRP (Fig. 8C). In addition, there were also similar changes in the tube formation capability, which confirms the initial activation of AG-5P for the capillary network formation response (Fig. 8D). A common bottleneck in clinical translation of hydrogel scaffolds lied in their limited internal vascularization, lacking effective blood vessel crawling. The above results suggest that PRP and other autologous bioactive substances may be an alternative solution to this problem.

The cellular behavior of macrophages is of much concern and a dynamic balance between immune response and regenerated signal during inflammatory phase is the prerequisite for the orderly development of the subsequent proliferation and remodeling phases. It has also been previously reported that activated PLTs could modulate macrophage polarization *in vitro* and *in vivo* [59]. Raw264.7 macrophages were co-cultured with negative control and 3D printed biolayer skin substitutes. LPS stimulation simulated the inflammatory microenvironment of the cutaneous wound, and whether the PRP-integrated constructs could play a role in inflammation regulation was assessed. As a result, the group of AG-5P showed less staining of iNOS and more staining of Arg-1 than the control and AG groups, which meant the integration of PRP could polarize macrophage to an anti-inflammatory M2 phenotype, while inhibit the pro-inflammatory polarization to M1 phenotype (Fig. 8E).

3.7. *In-situ 3D bioprinting repair of a rat dorsal full-thickness wound model*

3.7.1. *Improved wound healing rate and shortened epithelial gaps*

In-situ bioprinting has emerged as a powerful biofabrication technology with widespread applications in biomedical fields because of its superiority in high-throughput, high-precision, and individualized path planning. It judged the deposition layers according to the depth information of the tissue defect and delivered different cells for to repair the dermis and epidermis.

We next examined whether the PRP-integrated bioink was capable of *in-situ* bioprinting to improve wound healing in a full-thickness dermal dorsal defect model (Fig. 9). The *in-situ* manufacturing was carried out according to the Part 2.5.2 in a smooth process (Fig. 10 & Supplementary Video 2), with the composite bioinks adhering well to the wound beds. Macroscopic measurements of wound area showed the wound closure in AG-5P group was significantly superior when compared to the control and AG group (Fig. 11A–C). Contrasting to humans, the wound closure process of rodents is mainly via wound contraction, rather than granulation and epithelial regeneration [60]. We applied wound fixators (inner diameter of 20 mm) to objectively reflect the effect of *in-situ* bioprinting on human skin regeneration, however, resulting in a longer healing duration than allowing contractures. No signs of infection were present in any wound. In addition, HE staining was performed to assess the length of the remaining epithelial gaps, which confirmed the most adequate reepithelization and fastest wound closure of the AG-5P group (Fig. 11D and E).

Supplementary video related to this article can be found at https://doi.org/10.1016/j.mtbio.2022.100334

In an artificial tissue substitute, the exogenous matrix components are generally expected to serve as a reservoir for growth factors and to mediate cell-cell, cell-matrix, and matrix-protein interactions [61]. In the present 3D bioprinted constructs, the main network built by crosslinked gelatin took on this role. Integrated PRP entered the loose and porous structure, enriching the source of growth factors in the reservoir. This led to a biological cue that not only benefited the embedded seeded cells, but also modulated autologous repair signals through the material-wound interface.

3.7.2. *Regulatory effect on collagen synthesis and remodeling in vivo*

The deposition and arrangement of collagen fibers in the wound play an essential role in the reconstruction of wound structure and function and determine the quality of tissue remodeling, especially the possibility of scar formation [16] A promising bioactive substitute could improve the synthesis, directionality and composition of collagen during wound repair [29]. Masson's trichrome staining (MTS) and picrosirius red staining were performed on the repaired tissue after 1 week and 3 weeks (Fig. 12A). The quantitative results of MTS demonstrated a more extensive collagen deposition in the AG-5P group at both time points (Fig. 12B). This suggested that PRP could provide a favorable environment for tissue remodeling, which is also consistent with previous research [30]. In addition, the collagen assignment was reconstructed and organized in the AG and AG-5P groups after 3 weeks, while the control group was relatively disordered and sparse, which could be attributed to the orderly path of crosslinked bioink to guide the cell behavior of fibroblasts.

COL-1 fibers were stained red, whereas COL-3 fibers appeared green under polarized light microscopy. After the first week, the ratio of collagen I: III in the AG-5P and AG group was significantly reduced (Fig. 12C). While after 3 weeks, the AG-5P group still maintained a low ratio, but the AG group increased. Hence, the application of AG mainly promoted the synthesis of COL-1, and the integration of PRP not only increased the synthesis of total collagen, but also increased proportion of COL-3. Adult skin tissue is dominated by COL-1 and COL-3, with a higher proportion of COL-1, while the proportion of COL-3 in fetal skin tissue without scar healing is significantly higher than that in adults [62]. The collagen bundle formation in scar tissue is often accompanied by the massive transformation from COL-3 to COL-1 [63]. Therefore, the increase in the proportion of COL-3 is expected to enhance skin elasticity and reduce scar hyperplasia. Indeed, DFs play the key role in ECM synthesis as well as dermal contraction in line with the healing mechanism. However, the cell-based therapy tends to lose efficacy due to the hostile microenvironments of injured tissue. Studies have focused on the development of biomaterials that can not only deliver cells but also create the suitable microenvironment for the delivered and autologous cells. Based on the above outcomes, PRP may be an appropriate additive in bioinks to initiate the cellular functionality of DFs embedded in the dermal layer and the scar-inhibited biological cue.

3.8. *The integration of PRP could regulate the immune response during inflammation phase in wound healing after in-situ bioprinting*

Generally speaking, there would be an immune response after transplantation, which is most distinct in the inflammatory phase of wound repair, which is manifested locally by the infiltration of immune cells and the release of inflammatory cytokines [64]. Whether the inflammatory response at this stage is stable and controllable plays a vital role in the development of wound into regeneration or prolonged inflammation. Therefore, three major inflammatory cell markers (CD3 of T lymphocytes, MPO of neutrophils and CD68 of macrophages) were immunofluorescent stained on the day 3 of the wound (Fig. 13A). The lowest levels of CD3, CD68, and MPO were detected in the AG-5P groups compared with control and AG group, suggesting little sign of inflammation. Among them, the infiltration of $CD68^+$ macrophage in the AG-5P group was rich, although it was also significantly lower than the other two groups.

It has been well established that macrophages are key regulators of the wound healing process, with great plasticity in their phenotype and function, which could differentiate into either classically (M1) or activated (M2) macrophages based on the microenvironment. M2 phenotypic polarization plays an important role in promoting wound healing, especially neo-vascularization and tissue remodeling. As shown in Fig. 13B, there was a decreased number of iNOS$^+$ cells and an increased number of Arg-1$^+$ cells in the AG-5P group over the control and AG group. Our results showed that PRP incorporation significantly reduced macrophage infiltration into the 3D printed substitutes and promoted the polarization from M1 to M2 type macrophages. PRP was served as a homeostasis regulator to dynamically balance the immune response and tissue regeneration. A suppressed inflammation may modulate the subsequent wound healing stages of proliferation and remodeling [65], which we will discuss next.

3.9. The integration of PRP increased the blood perfusion of in-situ bioprinted skin substitutes

Studies [66] have shown that artificial scaffolds or skin substitutes need to have microvessels crawling in and establish blood perfusion within 1–2 weeks, otherwise the grafts may not survive. It could result in a pain of multiple operations for the patients and a poor healing effect. On day 14 of the wound, we applied LDPI to analyze the blood flow of the wound. In the AG and AG-PRP groups, Doppler signals were detected in the structures within the wound margin, reflecting the crawling of microvessels into the 3D printed constructs (Fig. 14). It's worth noting that positive signals were also detected in the wound center of the in the AG-5P group, indicating a higher degree of vascularization, and the artificial skin substitute was equipped with basic blood supply conditions inside.

Angiogenesis and neovascularization from the surrounding edges could facilitate the delivery of oxygen, nutrients and the infiltration of immune cell. IHC staining for CD31, a key vascular endothelial cell marker, was used to assess the newly formed blood vessels. Tubule-like structures positive for CD31 in AG-5P group were significantly higher than the other three groups on day 7. The quantification results validated such staining observations (Fig. 15A, C). The results were also consistent with the *in vitro* experiments on HUVECs. Furthermore, immunofluorescent double-label staining was performed for CD 31 to study the distribution of microvessels and stained for α-SMA to observe the mature vascular networks with smooth muscle cells (Fig. 15B, D). α-SMA-positive mature blood vessels were distributed in both *in-situ* printed healing groups, because the porous structure could provide a permissive microenvironment that supports lumen formation and vascular morphogenesis. And the AG-5P group exhibited the highest mature blood vessel density, which was critical for the rapid functionalization of *in-situ* printed constructs.

Several key growth factors were proven to be angiogenic factors that improve proliferation and differentiation of endothelial cells. Given that the development and maturation of new blood vessels is crucially dependent on the balanced spatiotemporal interaction of these factors, PRP was much more efficient in promoting formation of stable microvascular networks compared with the application of single recombinant growth factors [19]. It's reported that the platelets adhered to 3D engineered microvessels could enhance endothelial metabolic processes directly associated with glycolysis, which accounts for over 85% of the total cellular ATP production in endothelial cells in normal blood vessels [67]. The angiogenic effect of PRP could be attributed to the downregulation of the Notch signaling pathway in the angiogenic process [68]. Moreover, IL-6 was upregulated in wound treated with platelet-rich hydrogel over a longer period of time, which may be a driver to enhance vascularization in full thickness wounds [69].

Previous attempts on biomaterials modification normally focused on enhancing the biological activity at one stage of tissue repair and regeneration, while PRP integrated into a multi-component bioink endowed multiple biological cues to support the numerous stages, in a predefined spatial and temporal arrangement via *in-situ* bioprinting. This study utilized PRP for *in-situ* bioprinting for the first time, providing a promising strategy for development of biofunctional bioink and rapid fabrication for skin substitutes.

Although the above experiments have clearly demonstrated the superior feasibility of *in-situ* 3D bioprinting combined with PRP-functionalized bioink to accelerate wound healing, there are still some limitations. (1) studies with a large animal model with a long-term evaluation are warranted to confirm its clinical potential in future; (2) the precise molecular mechanism was not elucidated; (3) stem or precursor cells could be introduced into bioinks.

4. Conclusion

The requirements for seeded cell activity retention and construct-autologous tissue interaction for *in-situ* printing put forward higher standards for bioinks. Our data revealed that the integration of PRP at a concentration of 5% in the AG bioink had the strongest effect on improving the bioactivity *in vitro* and *in vivo*. The underlying mechanism of PRP incorporation within bioink for cutaneous wound healing is dynamic and complex, which runs through all stages of wound repair. It facilitated vital physiological processes including ECM synthesis, macrophage polarization, and angiogenesis, compared with unmodified AG bioink. This could be regarded as a typical case of multi-component bioink development. In clinical practice, patients' autologous PRP and cell suspension could be easily obtained at the bedside and during the operation. And we envision applying this strategy to perform bedside *in-situ* customized bioprinting during the operation to provide a new clinical treatment method in future.

Credit author statement

Ming Zhao: Writing - original draft, Writing – review & editing, Jing Wang: Data curation, Jinxin Zhang: Writing – review & editing, Jingman Huang: Software, Liang Luo: Software, Methodology, Yunshu Yang: Resources, Kuo Shen: Visualization, Tian Jiao: Writing - original draft, Yanhui Jia: Writing - original draft, Weilong Lian: Software, Jin Li: Methodology, Yunchuan Wang: Conceptualization, Funding acquisition, Qin Lian: Project administration, Dahai Hu: Conceptualization, Funding acquisition, Supervision.

Declaration of competing interest

The authors declare that they have no known competing financial interests or personal relationships that could have appeared to influence the work reported in this paper.

Acknowledgements

This work was supported by the Xijing Hospital Major Clinical Technology Innovation Projects [XJZT19Z03], and the National Natural Science Foundation of China [82172209, 81772071, 82172210, and 81772072].

Appendix A. Supplementary data

Supplementary data to this article can be found online at https://doi.org/10.1016/j.mtbio.2022.100334.

References

[1] Y. Belkaid, J.A. Segre, Dialogue between skin microbiota and immunity, Science 346 (6212) (2014) 954–959, https://doi.org/10.1126/science.1260144.
[2] M. Wang, Y. Luo, T. Wang, C. Wan, L. Pan, S. Pan, K. He, A. Neo, X. Chen, Artificial skin perception, Adv. Mater. 33 (19) (2021), 2003014, https://doi.org/10.1002/adma.202003014.

[3] Y. Yang, K. Huang, M. Wang, Q. Wang, H. Chang, Y. Liang, Q. Wang, J. Zhao, T. Tang, S. Yang, Ubiquitination flow repressors: enhancing wound healing of infectious diabetic ulcers through stabilization of polyubiquitinated hypoxia-inducible factor-1α by theranostic nitric oxide nanogenerators, Adv. Mater. 33 (45) (2021), 2103593, https://doi.org/10.1002/adma.202103593.
[4] Z. Zhu, D.W.H. Ng, H.S. Park, M.C. McAlpine, 3D-printed multifunctional materials enabled by artificial-intelligence-assisted fabrication technologies, Nat. Rev. Mater. 6 (1) (2021) 27–47, https://doi.org/10.1038/s41578-020-00235-2.
[5] C. Mota, S. Camarero-Espinosa, M.B. Baker, P. Wieringa, L. Moroni, Bioprinting: from tissue and organ development to models, Chem. Rev. 120 (19) (2020) 10547–10607, https://doi.org/10.1021/acs.chemrev.9b00789.
[6] S.V. Murphy, P. De Coppi, A. Atala, Opportunities and challenges of translational 3D bioprinting, Nat. Biomed. Eng. 4 (4) (2020) 370–380, https://doi.org/10.1038/s41551-019-0471-7.
[7] S.M. Hull, L.G. Brunel, S.C. Heilshorn, 3D bioprinting of cell-laden hydrogels for improved biological functionality, Adv. Mater. 34 (2) (2021), e2103691, https://doi.org/10.1002/adma.202103691.
[8] C. Zhou, Y. Yang, J. Wang, Q. Wu, Z. Gu, Y. Zhou, X. Liu, Y. Yang, H. Tang, Q. Ling, L. Wang, J. Zang, Ferromagnetic soft catheter robots for minimally invasive bioprinting, Nat. Commun. 12 (1) (2021) 5072, https://doi.org/10.1038/s41467-021-25386-w.
[9] F. Agostinacchio, X. Mu, S. Dirè, A. Motta, D.L. Kaplan, In situ 3D printing: opportunities with silk inks, Trends Biotechnol. 39 (7) (2021) 719–730, https://doi.org/10.1016/j.tibtech.2020.11.003.
[10] K. Ma, T. Zhao, L. Yang, P. Wang, J. Jin, H. Teng, D. Xia, L. Zhu, L. Li, Q. Jiang, X. Wang, Application of robotic-assisted 3D printing in cartilage regeneration with HAMA hydrogel: an study, J. Adv. Res. 23 (2020) 123–132, https://doi.org/10.1016/j.jare.2020.01.010.
[11] S. Singh, D. Choudhury, F. Yu, V. Mironov, M.W. Naing, In situ bioprinting - bioprinting from benchside to bedside? Acta Biomater. 101 (2020) 14–25, https://doi.org/10.1016/j.actbio.2019.08.045.
[12] J. Groll, J.A. Burdick, D.W. Cho, B. Derby, M. Gelinsky, S.C. Heilshorn, T. Jüngst, J. Malda, V.A. Mironov, K. Nakayama, A. Ovsianikov, W. Sun, S. Takeuchi, J.J. Yoo, T.B.F. Woodfield, A definition of bioinks and their distinction from biomaterial inks, Biofabrication 11 (1) (2018), 013001, https://doi.org/10.1088/1758-5090/aaec52.
[13] X. Cui, J. Li, Y. Hartanto, M. Durham, J. Tang, H. Zhang, G. Hooper, K. Lim, T. Woodfield, Advances in extrusion 3D bioprinting: a focus on multicomponent hydrogel-based bioinks, Adv. Healthc. Mater. 9 (15) (2020), e1901648, https://doi.org/10.1002/adhm.201901648.
[14] A.C. Daly, M.E. Prendergast, A.J. Hughes, J.A. Burdick, Bioprinting for the biologist, Cell 184 (1) (2021) 18–32, https://doi.org/10.1016/j.cell.2020.12.002.
[15] S. Heid, A.R. Boccaccini, Advancing bioinks for 3D bioprinting using reactive fillers: a review, Acta Biomater. 113 (2020), https://doi.org/10.1016/j.actbio.2020.06.040.
[16] Y. Huyan, Q. Lian, T. Zhao, D. Li, J. He, Pilot study of the biological properties and vascularization of 3D printed bilayer skin grafts, Int. J. Bioprint. 6 (1) (2020) 246, https://doi.org/10.18063/ijb.v6i1.246.
[17] Q. Lian, T. Zhao, T. Jiao, Y. Huyan, H. Gu, L. Gao, Direct-writing process and in vivo evaluation of prevascularized composite constructs for muscle tissue engineering application, J. Bionic Eng. 17 (3) (2020) 457–468, https://doi.org/10.1007/s42235-020-0037-0.
[18] P. Rastogi, B. Kandasubramanian, Review of alginate-based hydrogel bioprinting for application in tissue engineering, Biofabrication 11 (4) (2019), 042001, https://doi.org/10.1088/1758-5090/ab331e.
[19] M.W. Laschke, M.D. Menger, The simpler, the better: tissue vascularization using the body's own resources, Trends Biotechnol. 40 (3) (2022) 281–290, https://doi.org/10.1016/j.tibtech.2021.07.002.
[20] J.N. Katz, Platelet-rich plasma for osteoarthritis and achilles tendinitis, JAMA 326 (20) (2021) 2012–2014, https://doi.org/10.1001/jama.2021.19540.
[21] P. Gentile, S. Garcovich, Systematic review: adipose-derived mesenchymal stem cells, platelet-rich plasma and biomaterials as new regenerative strategies in chronic skin wounds and soft tissue defects, Int. J. Mol. Sci. 22 (4) (2021), https://doi.org/10.3390/ijms22041538.
[22] P. Gentile, S. Garcovich, Autologous activated platelet-rich plasma (AA-PRP) and non-activated (A-PRP) in hair growth: a retrospective, blinded, randomized evaluation in androgenetic alopecia, Expet Opin. Biol. Ther. 20 (3) (2020) 327–337, https://doi.org/10.1080/14712598.2020.1724951.
[23] M. Alam, R. Hughart, A. Champlain, A. Geisler, K. Paghdal, D. Whiting, J.A. Hammel, A. Maisel, M.J. Rapcan, D.P. West, E. Poon, Effect of platelet-rich plasma injection for rejuvenation of photoaged facial skin: a randomized clinical trial, JAMA Dermatol. 154 (12) (2018) 1447–1452, https://doi.org/10.1001/jamadermatol.2018.3977.
[24] M. Hesseler, N. Shyam, Platelet-rich plasma and its utility in medical dermatology: a systematic review, J. Am. Acad. Dermatol. 81 (3) (2019) 834–846, https://doi.org/10.1016/j.jaad.2019.04.037.
[25] P. Gentile, M.G. Scioli, A. Bielli, A. Orlandi, V. Cervelli, Concise review: the use of adipose-derived stromal vascular fraction cells and platelet rich plasma in regenerative plastic surgery, Stem Cells (Dayton) 35 (1) (2017) 117–134, https://doi.org/10.1002/stem.2498.
[26] N. Faramarzi, I.K. Yazdi, M. Nabavinia, A. Gemma, A. Fanelli, A. Caizzone, L.M. Ptaszek, I. Sinha, A. Khademhosseini, J.N. Ruskin, A. Tamayol, Patient-specific bioinks for 3D bioprinting of tissue engineering scaffolds, Adv. Healthc. Mater. 7 (11) (2018), e1701347, https://doi.org/10.1002/adhm.201701347.
[27] B. Qian, Q. Yang, M. Wang, S. Huang, C. Jiang, H. Shi, Q. Long, M. Zhou, Q. Zhao, X. Ye, Encapsulation of lyophilized platelet-rich fibrin in alginate-hyaluronic acid hydrogel as a novel vascularized substitution for myocardial infarction, Bioact. Mater. 7 (2022) 401–411, https://doi.org/10.1016/j.bioactmat.2021.05.042.
[28] D.W. Long, N.R. Johnson, E.M. Jeffries, H. Hara, Y. Wang, Controlled delivery of platelet-derived proteins enhances porcine wound healing, J. Contr. Release 253 (2017) 73–81, https://doi.org/10.1016/j.jconrel.2017.03.021.
[29] M. Rodrigues, N. Kosaric, C.A. Bonham, G.C. Gurtner, Wound healing: a cellular perspective, Physiol. Rev. 99 (1) (2019) 665–706, https://doi.org/10.1152/physrev.00067.2017.
[30] S. Mahmoudi, E. Mancini, L. Xu, A. Moore, F. Jahanbani, K. Hebestreit, R. Srinivasan, X. Li, K. Devarajan, L. Prélot, C.E. Ang, Y. Shibuya, B.A. Benayoun, A.L.S. Chang, M. Wernig, J. Wysocka, M.T. Longaker, M.P. Snyder, A. Brunet, Heterogeneity in old fibroblasts is linked to variability in reprogramming and wound healing, Nature 574 (7779) (2019) 553–558, https://doi.org/10.1038/s41586-019-1658-5.
[31] Z. Lin, C. Zhao, Z. Lei, Y. Zhang, R. Huang, B. Lin, Y. Dong, H. Zhang, J. Li, X. Li, Epidermal stem cells maintain stemness via a biomimetic micro/nanofiber scaffold that promotes wound healing by activating the Notch signaling pathway, Stem Cell Res. Ther. 12 (1) (2021) 341, https://doi.org/10.1186/s13287-021-02418-2.
[32] Y. Liang, X. Zhao, T. Hu, B. Chen, Z. Yin, P.X. Ma, B. Guo, Adhesive hemostatic conducting injectable composite hydrogels with sustained drug release and photothermal antibacterial activity to promote full-thickness skin regeneration during wound healing, Small 15 (12) (2019), e1900046, https://doi.org/10.1002/smll.201900046.
[33] M. Li, Y. Liang, J. He, H. Zhang, B. Guo, Two-pronged strategy of biomechanically active and biochemically multifunctional hydrogel wound dressing to accelerate wound closure and wound healing, Chem. Mater. 32 (23) (2020) 9937–9953, https://doi.org/10.1021/acs.chemmater.0c02823.
[34] H. Wang, Q. Lian, D. Li, C. Li, T. Zhao, J. Liang, Multi-tissue layering and path planning of in situ bioprinting for complex skin and soft tissue defects, Rapid Prototyp. J. 27 (2) (2021) 321–332, https://doi.org/10.1108/RPJ-08-2020-0201.
[35] Q. Zhang, T. Yang, R. Zhang, X. Liang, G. Wang, Y. Tian, L. Xie, W. Tian, Platelet lysate functionalized gelatin methacrylate microspheres for improving angiogenesis in endodontic regeneration, Acta Biomater. (2021), https://doi.org/10.1016/j.actbio.2021.09.024.
[36] C. Wang, M. Wang, T. Xu, X. Zhang, C. Lin, W. Gao, H. Xu, B. Lei, C. Mao, Engineering bioactive self-healing antibacterial exosomes hydrogel for promoting chronic diabetic wound healing and complete skin regeneration, Theranostics 9 (1) (2019) 65–76, https://doi.org/10.7150/thno.29766.
[37] A. Shafiee, A.S. Cavalcanti, N.T. Saidy, D. Schneidereit, O. Friedrich, A. Ravichandran, E.M. De-Juan-Pardo, D.W. Hutmacher, Convergence of 3D printed biomimetic wound dressings and adult stem cell therapy, Biomaterials 268 (2021), 120558, https://doi.org/10.1016/j.biomaterials.2020.120558.
[38] V.R. Thangapandi, O. Knittelfelder, M. Brosch, E. Patsenker, O. Vvedenskaya, S. Buch, S. Hinz, A. Hendricks, M. Nati, A. Herrmann, D.R. Rekhade, T. Berg, M. Matz-Soja, K. Huse, E. Klipp, J.K. Pauling, J.A.H. Wodke, J. Miranda Ackerman, M.v. Bonin, E. Aigner, C. Datz, W. von Schönfels, S. Nehring, S. Zeissig, C. Röcken, A. Dahl, T. Chavakis, F. Stickel, A. Shevchenko, C. Schafmayer, J. Hampe, P. Subramanian, Loss of hepatic Mboat7 leads to liver fibrosis, Gut 70 (5) (2021) 940, https://doi.org/10.1136/gutjnl-2020-320853.
[39] M. Samberg, R. Stone, S. Natesan, A. Kowalczewski, S. Becerra, N. Wrice, A. Cap, R. Christy, Platelet rich plasma hydrogels promote in vitro and in vivo angiogenic potential of adipose-derived stem cells, Acta Biomater. 87 (2019) 76–87, https://doi.org/10.1016/j.actbio.2019.01.039.
[40] E. Anitua, P. Nurden, R. Prado, A.T. Nurden, S. Padilla, Autologous fibrin scaffolds: when platelet- and plasma-derived biomolecules meet fibrin, Biomaterials 192 (2019) 440–460, https://doi.org/10.1016/j.biomaterials.2018.11.029.
[41] A. Gazendam, S. Ekhtiari, A. Bozzo, M. Phillips, M. Bhandari, Intra-articular saline injection is as effective as corticosteroids, platelet-rich plasma and hyaluronic acid for hip osteoarthritis pain: a systematic review and network meta-analysis of randomised controlled trials, Br. J. Sports Med. 55 (5) (2021) 256, https://doi.org/10.1136/bjsports-2020-102179.
[42] K. Liu, M. Zhao, Y. Li, L. Luo, D. Hu, VEGF loaded porcine decellularized adipose tissue derived hydrogel could enhance angiogenesis in vitro and in vivo, J. Biomater. Sci. Polym. Ed. (2021) 1–13, https://doi.org/10.1080/09205063.2021.2002235.
[43] G. Jiang, S. Li, K. Yu, B. He, J. Hong, T. Xu, J. Meng, C. Ye, Y. Chen, Z. Shi, G. Feng, W. Chen, S. Yan, Y. He, R. Yan, A 3D-printed PRP-GelMA hydrogel promotes osteochondral regeneration through M2 macrophage polarization in a rabbit model, Acta Biomater. (2021), https://doi.org/10.1016/j.actbio.2021.04.010.
[44] K. Fukada, T. Tajima, M. Seyama, Thermoresponsive gelatin/chitosan hydrogel films for a degradable capacitor, ACS Appl. Mater. Interfaces 13 (49) (2021) 59006–59011, https://doi.org/10.1021/acsami.1c14905.
[45] T. Hu, X. Cui, M. Zhu, M. Wu, Y. Tian, B. Yao, W. Song, Z. Niu, S. Huang, X. Fu, 3D-printable supramolecular hydrogels with shear-thinning property: fabricating strength tunable bioink via dual crosslinking, Bioact. Mater. 5 (4) (2020) 808–818, https://doi.org/10.1016/j.bioactmat.2020.06.001.
[46] B. Yao, T. Hu, X. Cui, W. Song, X. Fu, S. Huang, Enzymatically degradable alginate/gelatin bioink promotes cellular behavior and degradation in vitro and in vivo, Biofabrication 11 (4) (2019), 045020, https://doi.org/10.1088/1758-5090/ab38ef.
[47] J. Chu, P. Shi, W. Yan, J. Fu, Z. Yang, C. He, X. Deng, H. Liu, PEGylated graphene oxide-mediated quercetin-modified collagen hybrid scaffold for enhancement of MSCs differentiation potential and diabetic wound healing, Nanoscale 10 (20) (2018) 9547–9560, https://doi.org/10.1039/c8nr02538j.
[48] H. Zhu, J. Li, Y. Li, Z. Zheng, H. Guan, H. Wang, K. Tao, J. Liu, Y. Wang, W. Zhang, C. Li, J. Li, L. Jia, W. Bai, D. Hu, Glucocorticoid counteracts cellular

mechanoresponses by LINC01569-dependent glucocorticoid receptor-mediated mRNA decay, Sci. Adv. 7 (9) (2021), https://doi.org/10.1126/sciadv.abd9923.
[49] J. Zonderland, L. Moroni, Steering cell behavior through mechanobiology in 3D: a regenerative medicine perspective, Biomaterials 268 (2021), 120572, https://doi.org/10.1016/j.biomaterials.2020.120572.
[50] R.J.F.C. do Amaral, N.M.A. Zayed, E.I. Pascu, B. Cavanagh, C. Hobbs, F. Santarella, C.R. Simpson, C.M. Murphy, R. Sridharan, A. González-Vázquez, B. O'Sullivan, F.J. O'Brien, C.J. Kearney, Functionalising collagen-based scaffolds with platelet-rich plasma for enhanced skin wound healing potential, Front. Bioeng. Biotechnol. 7 (2019) 371, https://doi.org/10.3389/fbioe.2019.00371.
[51] P. Gentile, S. Garcovich, Systematic review-the potential implications of different platelet-rich plasma (PRP) concentrations in regenerative medicine for tissue repair, Int. J. Mol. Sci. 21 (16) (2020), https://doi.org/10.3390/ijms21165702.
[52] E. Rognoni, A.O. Pisco, T. Hiratsuka, K.H. Sipilä, J.M. Belmonte, S.A. Mobasseri, C. Philippeos, R. Dilão, F.M. Watt, Fibroblast state switching orchestrates dermal maturation and wound healing, Mol. Syst. Biol. 14 (8) (2018), e8174, https://doi.org/10.15252/msb.20178174.
[53] Q. Wen, S.M. Mithieux, A.S. Weiss, Elastin biomaterials in dermal repair, Trends Biotechnol. 38 (3) (2020) 280–291, https://doi.org/10.1016/j.tibtech.2019.08.005.
[54] D. Yoon, Y.S. Cho, S.Y. Joo, C.H. Seo, Y.S. Cho, A clinical trial with a novel collagen dermal substitute for wound healing in burn patients, Biomater. Sci. 8 (3) (2020) 823–829, https://doi.org/10.1039/C9BM01209E.
[55] J.Q. Coentro, E. Pugliese, G. Hanley, M. Raghunath, D.I. Zeugolis, Current and upcoming therapies to modulate skin scarring and fibrosis, Adv. Drug Deliv. Rev. 146 (2019) 37–59, https://doi.org/10.1016/j.addr.2018.08.009.
[56] M.S. Hu, W.X. Hong, M. Januszyk, G.G. Walmsley, A. Luan, Z.N. Maan, S. Moshrefi, R. Tevlin, D.C. Wan, G.C. Gurtner, M.T. Longaker, H.P. Lorenz, Pathway analysis of gene expression in murine fetal and adult wounds, Adv. Wound Care 7 (8) (2018) 262–275, https://doi.org/10.1089/wound.2017.0779.
[57] X. Liu, Y. Yang, X. Niu, Q. Lin, B. Zhao, Y. Wang, L. Zhu, An in situ photocrosslinkable platelet rich plasma - complexed hydrogel glue with growth factor controlled release ability to promote cartilage defect repair, Acta Biomater. 62 (2017) 179–187, https://doi.org/10.1016/j.actbio.2017.05.023.
[58] J. Ma, C. Qin, J. Wu, H. Zhang, H. Zhuang, M. Zhang, Z. Zhang, L. Ma, X. Wang, B. Ma, J. Chang, C. Wu, 3D printing of strontium silicate microcylinder-containing multicellular biomaterial inks for vascularized skin regeneration, Adv. Healthc. Mater. 10 (16) (2021), 2100523, https://doi.org/10.1002/adhm.202100523.
[59] F.S. Al-Hamed, L. Abu-Nada, R. Rodan, S. Sarrigiannidis, J.L. Ramirez-Garcialuna, H. Moussa, O. Elkashty, Q. Gao, T. Basiri, L. Baca, J. Torres, L. Rancan, S.D. Tran, M. Lordkipanidzé, M. Kaartinen, Z. Badran, F. Tamimi, Differences in platelet-rich plasma composition influence bone healing, J. Clin. Periodontol. 48 (12) (2021) 1613–1623, https://doi.org/10.1111/jcpe.13546.
[60] W.A. Dorsett-Martin, Rat models of skin wound healing: a review, Wound Repair Regen. 12 (6) (2004) 591–599, https://doi.org/10.1111/j.1067-1927.2004.12601.x.
[61] S. He, J. Fang, C. Zhong, F. Ren, M. Wang, Controlled pVEGF delivery via a gene-activated matrix comprised of a peptide-modified non-viral vector and a nanofibrous scaffold for skin wound healing, Acta Biomater. 140 (2021) 149–162, https://doi.org/10.1016/j.actbio.2021.11.037.
[62] M. Monavarian, S. Kader, S. Moeinzadeh, E. Jabbari, Regenerative scar-free skin wound healing, Tissue Eng. B Rev. 25 (4) (2019) 294–311, https://doi.org/10.1089/ten.TEB.2018.0350.
[63] D. Avery, P. Govindaraju, M. Jacob, L. Todd, J. Monslow, E. Puré, Extracellular matrix directs phenotypic heterogeneity of activated fibroblasts, Matrix Biol. 67 (2018), https://doi.org/10.1016/j.matbio.2017.12.003.
[64] T. Win, W. Crisler, B. Dyring-Andersen, R. Lopdrup, J. Teague, Q. Zhan, V. Barrera, S. Ho Sui, S. Tasigiorgos, N. Murakami, A. Chandraker, S. Tullius, B. Pomahac, L. Riella, Clark, R. J. T. J. o. c. i., Immunoregulatory and lipid presentation pathways are upregulated in human face transplant rejection, J. Clin. Investig. 131 (8) (2021), https://doi.org/10.1172/jci135166.
[65] N.X. Landén, D. Li, M. Ståhle, Transition from inflammation to proliferation: a critical step during wound healing, Cell. Mol. Life Sci. 73 (20) (2016) 3861–3885, https://doi.org/10.1007/s00018-016-2268-0.
[66] L. Chen, Q. Xing, Q. Zhai, M. Tahtinen, F. Zhou, L. Chen, Y. Xu, S. Qi, F. Zhao, Pre-vascularization enhances therapeutic effects of human mesenchymal stem cell sheets in full thickness skin wound repair, Theranostics 7 (1) (2017) 117–131, https://doi.org/10.7150/thno.17031.
[67] R.J. Nagao, R. Marcu, Y. Wang, L. Wang, C. Arakawa, C. DeForest, J. Chen, J.A. López, Y. Zheng, Transforming endothelium with platelet-rich plasma in engineered microvessels, Adv. Sci. 6 (24) (2019), 1901725, https://doi.org/10.1002/advs.201901725.
[68] N. Ebrahim, A.A. Dessouky, O. Mostafa, A. Hassouna, M.M. Yousef, Y. Seleem, E.A.E.A.M. El Gebaly, M.M. Allam, A.S. Farid, B.A. Saffaf, D. Sabry, A. Nawar, A.A. Shoulah, A.H. Khalil, S.F. Abdalla, M. El-Sherbiny, N.M. Elsherbiny, R.F. Salim, Adipose mesenchymal stem cells combined with platelet-rich plasma accelerate diabetic wound healing by modulating the Notch pathway, Stem Cell Res. Ther. 12 (1) (2021) 392, https://doi.org/10.1186/s13287-021-02454-y.
[69] M.M. Rahman, N. Garcia, Y.S. Loh, D.C. Marks, I. Banakh, P. Jagadeesan, N.R. Cameron, C. Yung-Chih, M. Costa, K. Peter, H. Cleland, S. Akbarzadeh, A platelet-derived hydrogel improves neovascularisation in full thickness wounds, Acta Biomater. 136 (2021) 199–209, https://doi.org/10.1016/j.actbio.2021.09.043.